



HAL
open science

Protection of NO_x Sensors from Sulfur Poisoning in Glass Furnaces by the Optimization of a “SO₂ Trap”

Carole Naddour, Mathilde Rieu, A. Boreave, S. Gil, P. Vernoux, Jean-Paul Viricelle

► **To cite this version:**

Carole Naddour, Mathilde Rieu, A. Boreave, S. Gil, P. Vernoux, et al.. Protection of NO_x Sensors from Sulfur Poisoning in Glass Furnaces by the Optimization of a “SO₂ Trap”. *Sensors*, 2023, 23 (19), pp.8186. 10.3390/s23198186. emse-04233545

HAL Id: emse-04233545

<https://hal-emse.ccsd.cnrs.fr/emse-04233545v1>

Submitted on 9 Oct 2023

HAL is a multi-disciplinary open access archive for the deposit and dissemination of scientific research documents, whether they are published or not. The documents may come from teaching and research institutions in France or abroad, or from public or private research centers.




L'archive ouverte pluridisciplinaire **HAL**, est destinée au dépôt et à la diffusion de documents scientifiques de niveau recherche, publiés ou non, émanant des établissements d'enseignement et de recherche français ou étrangers, des laboratoires publics ou privés.



Distributed under a Creative Commons Attribution 4.0 International License

Article

Protection of NO_x Sensors from Sulfur Poisoning in Glass Furnaces by the Optimization of a “SO₂ Trap”

Carole Naddour ^{1,2}, Mathilde Rieu ^{1,*} , Antoinette Boreave ², Sonia Gil ² , Philippe Vernoux ² and Jean-Paul Viricelle ¹ 

¹ Mines Saint-Etienne, Univ Lyon, CNRS, UMR 5307 LGF, Centre SPIN, F-42023 Saint-Etienne, France; carole.naddour@emse.fr (C.N.); viricelle@emse.fr (J.-P.V.)

² Univ Lyon, Université Lyon 1, CNRS, UMR 5256, IRCELYON, 2 avenue Albert Einstein, F-69622 Villeurbanne, France; antoinette.boreave@ircelyon.univ-lyon1.fr (A.B.); sonia.gil@ircelyon.univ-lyon1.fr (S.G.); philippe.vernoux@ircelyon.univ-lyon1.fr (P.V.)

* Correspondence: rieu@emse.fr

Abstract: Electrochemical NO_x sensors based on yttria-stabilized zirconia (YSZ) provide a reliable onboard way to control NO_x emissions from glass-melting furnaces. The main limitation is the poisoning of this sensor by sulfur oxides (SO_x) contained in the stream. To overcome this drawback, an “SO₂ trap” with high SO_x storage capacity and low affinity to NO_x is required. Two CuO/BaO/SBA-15 traps with the same CuO loading (6.5 wt.%) and different BaO loadings (5 and 24.5 wt.%, respectively) were synthesized, thoroughly characterized and evaluated as SO₂ traps. The results show that the 6.5%CuO/5%BaO/SBA-15 trap displays the highest SO₂ adsorption capacity and can fully adsorb SO₂ for a specific period of time, while additionally displaying a very low NO adsorption capacity. A suitable quantity of this material located upstream of the sensor could provide total protection of the NO_x sensor against sulfur poisoning in glass-furnace exhausts.

Keywords: NO_x sensor; glass furnaces; sulfur poisoning; SO₂ trap; CuO/BaO-based traps



Citation: Naddour, C.; Rieu, M.; Boreave, A.; Gil, S.; Vernoux, P.; Viricelle, J.-P. Protection of NO_x Sensors from Sulfur Poisoning in Glass Furnaces by the Optimization of a “SO₂ Trap”. *Sensors* **2023**, *23*, 8186. <https://doi.org/10.3390/s23198186>

Academic Editors: Rosamaria Capuano and Alexandro Catini

Received: 1 September 2023

Revised: 27 September 2023

Accepted: 28 September 2023

Published: 30 September 2023



Copyright: © 2023 by the authors. Licensee MDPI, Basel, Switzerland. This article is an open access article distributed under the terms and conditions of the Creative Commons Attribution (CC BY) license (<https://creativecommons.org/licenses/by/4.0/>).

1. Introduction

Nitrous oxides (NO_x) are well known as extremely harmful pollutants that play key roles in the generation of acid rain and photochemical smog and cause damage to human health [1]. In glass-melting furnaces, the combustion of natural gas, heavy oils, and other fuel sources is used to melt raw materials at high process temperatures of up to 1500 °C, resulting in NO_x emissions in the exhaust gas [2,3]. Many countries and organizations have imposed stringent emission regulations on glass furnaces to reduce their NO_x pollution levels. In this respect, the development of in situ, cheap and robust techniques, like NO_x sensors, becomes urgent for the onboard control of NO_x emissions during the combustion processes [1,4]. Electrochemical sensors based on a solid electrolyte are a promising method for the detection of NO_x. They have been extensively studied due to their high sensitivity, selectivity, and durability. In this paper, we will only focus on the potentiometric gas sensor based on yttria-stabilized zirconia (YSZ) solid electrolyte, as reported by many research groups [5–11]. For example, Ferlazzo et al. [12] developed an electrochemical biosensor based on YSZ for amino acid detection. Ando et al. [13] studied a capacitive biosensor using a YSZ functional layer for the quantification of ammonia. Hao et al. [14] used a YSZ-based potentiometric sensor with ZnGa₂O₄ and Pt electrodes for the detection of SO₂ under harsh environments with a high sensitivity. The YSZ-based sensors are generally distinguished by their high temperature resistance and high chemical stability, in addition to good and reproducible sensing performance [15].

Usually, a platinum reference electrode and a gold sensing electrode are associated with the YSZ electrolyte. The signal of this sensor type ($\Delta V = V_{Pt} - V_{Au}$) in a complex gas

environment is based on the development of a mixed potential on the sensing electrode, as described in previous studies [16–18].

One of the major challenges in NO_x sensors is the cross-sensitivity to other pollutants such as CO, as well as the hydrocarbons present in the exhaust. In order to eliminate this interference with untargeted gases and to obtain a higher NO_x selectivity, a solution proposed in the literature is to use a catalytic filter [19–21] on top of the sensing electrode. For instance, Gao et al. [6,22] have developed a NO_x-selective Pt/YSZ/Au sensor by coating a catalytic filter consisting of 1.7–4.5 wt.% Pt dispersed on alumina directly on the sensing elements of the sensor. They reported that this filter can fully oxidize CO and hydrocarbons, and thereby remove their interference. In addition, the catalytic filter allows for the reaching of the NO/NO₂ thermodynamic equilibrium, resulting in a similar response for either NO or NO₂ at equal concentrations. Therefore, the sensor response depends only on the total NO_x concentration, regardless of the NO/NO₂ ratio arriving at the sensor, at a constant oxygen partial-pressure and temperature. Another way to obtain selective and sensitive sensors is to apply a polarization current. Some studies reported that the polarization of the sensing electrode can control the selectivity of the sensor towards NO or NO₂ [23–25]. J.P. Viricelle et al. [26] have proposed a sensitive three-electrode sensor based on the selective electrochemical reduction of NO₂. In this study, the YSZ-based electrochemical cell operates upon electric polarization between an Au working electrode and a Pt counter-electrode, resulting in selective NO₂ detection at 400–550 °C. When the Au working electrode is negatively polarized, only reducible gas (NO₂) can affect its potential (at constant oxygen partial pressure) and therefore be detected, which avoids interference from reductive gases such as CO hydrocarbons. To achieve a selective and sensitive response to NO_x and not only NO₂, the idea of GaO et al. [22] was to combine both the catalytic filter and the electrical polarization on a three-electrode sensor.

However, for glass-melting furnace applications, one of the main issues is the presence of sulfur oxides (SO_x) in the stream, which can significantly poison the electrodes and the Pt/Al₂O₃ catalytic filter of the NO_x sensor [27,28]. Therefore, this study aims to develop a sulfur oxides “trap” located up-stream from the sensor to protect the NO_x sensors from sulfur poisoning. Such material must exhibit a good catalytic activity for the oxidation of SO₂ to SO₃ and a high SO_x storage capacity into sulfates. Furthermore, the overall NO_x concentration in the stream must not be altered, excluding the NO_x storage on the trap material. A large variety of materials have been reported as potential SO_x traps, and can be classified in different categories such as single-oxides materials (CaO, MgO, TiO₂, MnO₂, CeO₂, Al₂O₃), oxides supported on porous silica or alumina-based materials (zeolites, mesoporous or clay minerals) and oxides supported on carbonaceous materials (activated carbon and carbon fibers) [29–37]. Al₂O₃-based oxides undergo sulfation leading to a loss in their textural properties [38] and present a specific surface area (SSA) in the order of 200 m²/g, which is not high enough for this application. The main drawback of activated carbons is their limited thermal stability [39]. On the other hand, organized mesoporous silica SBA-15 could be a suitable support, combining a high thermal stability with a chemical inertia towards SO_x, which was shown to protect the mesoporous structure from collapsing [38,40]. Moreover, SBA-15 presents a high SSA and porous volume that can highly disperse the SO_x-storage active phases [41,42]. Many studies are focused on SO_x traps based on copper oxide (CuO) as an active phase [38,43–49]. Xue et al. [50] found that among a series of adsorbents (CuO, Zn/Mn type, Zn/Ti/Zr type, Zn/Co type, and Zn/Al type), the CuO-based adsorbents exhibited higher reactivity levels for low-temperature desulfurization. Indeed, this oxide exhibits a significant catalytic activity towards the oxidation of SO₂ to SO₃ and a good ability to store SO₃ as CuSO₄. In addition, CuO can be easily regenerated after the decomposition of CuSO₄ at a relatively low temperature (<700 °C), thereby limiting the energy consumption and preventing the support deterioration. Furthermore, SO₂ released during the regeneration step can be recovered as sulfuric acid or pure sulfur [51,52].

On the other hand, BaO is a well-known NO_x storage compound involved in NO_x storage/reduction (NSR) catalysts developed for the post-treatment of diesel vehicles [53–55]. However, its deactivation by sulfur species is well documented in the literature [27,28,56]. For example, the SO₂ exposure of Pt/BaO/Al₂O₃ and Pt/BaCO₃/Al₂O₃ catalysts, used as NO_x traps, has resulted in the formation of surface and bulk sulfates on barium sites.

Indeed, BaO has a high ability for sulfation under harsh environments, and the resulting barium sulfates are more stable than barium nitrates [55,56]. Moreover, since the storage capacity depends on the experimental conditions, especially on the reaction temperature, it seems possible to make the SO_x adsorption predominant with respect to that of NO_x on BaO sites. However, BaO is not active for the oxidation of SO₂ to SO₃ and cannot be used as the sole active phase in the catalyst. In this context, in addition to CuO, BaO was chosen as a second active phase to further increase the SO_x storage capacity.

In this work, the SO₂ storage capacity of two CuO/BaO/SBA-15 adsorbents with different BaO loadings were assessed under simulated gases from glass-furnace exhaust during multicycle experiments. These traps were characterized by the inductively coupled plasma method (ICP), X-ray diffraction (XRD), N₂ physisorption, laser diffraction granulometry, and scanning electron microscopy (SEM). The performances of potentiometric NO_x sensors were also investigated when coupled, or not, with an upstream SO₂ trap. Moreover, the presence of sulfites/sulfate species on the most efficient adsorbent after several cycles of NO-SO₂ exposures was confirmed by diffuse reflectance infrared Fourier transform spectroscopy (DRIFTS).

2. Materials and Methods

2.1. Synthesis of CuO/BaO/SBA-15 Traps

A commercial SBA-15 mesoporous silica (XFNANO) was first calcined at 900 °C for 2 h with a ramp of 10 °C/min in static air. The CuO/BaO/SBA-15 SO₂ traps were prepared as follows. First, CuO was wet-impregnated on the pre-calcined SBA support: the targeted amount of Cu(NO₃)₂·3H₂O (Sigma-Aldrich, Massachusetts, United States) precursor was dissolved in 40 mL of distilled water, in which 4.4 g of the pre-calcined SBA-15 support had been added under stirring at room temperature for few minutes. This mixture was then heated at 65 °C, under stirring, until the complete evaporation of the water. The resulting powder was dried overnight at 80 °C in an oven and then calcined in a tubular reactor at 600 °C for 5 h with a ramp of 2 °C/min under synthetic air flow (10 L/h). BaO was also wet-impregnated on the prepared CuO/SBA-15 powder by using Ba(CH₃COO)₂ (Sigma-Aldrich) as a precursor and following the same synthesis steps. Two CuO/BaO/SBA-15 adsorbents with the same CuO amount (6.5 wt.%) and different BaO loadings (5 and 24.5 wt.%) were prepared using this protocol.

2.2. Characterization Techniques

The chemical composition of the SO₂ traps was determined by inductively coupled plasma-optical emission spectrometer (ICP-OES), using a HORIBA Jobin Yvon-Activa spectrometer, from powders previously dissolved in a mixture of inorganic acids (HNO₃ and HF).

X-ray powder diffraction (XRD) was performed in reflection mode on a Bruker D8-A25 diffractometer (Cu K α radiation, $\lambda = 1.5406 \text{ \AA}$) equipped with a LYNXEYE XE-T linear detector. Wide-angle measurements were achieved for 2θ angle values in the 5–80° range, by steps of 0.04°. For low-angle measurements (2θ range from 0.45 to 7°, by steps of 0.01°, with a time of 118 s per step), a second XRD apparatus was used, the Bruker AXS diffractometer (Cu-K α radiation, $\lambda = 1.54184 \text{ \AA}$) equipped with a LYNXEYE detector.

N₂ physisorption analyses were performed on a Micromeritics Tristar 3000 apparatus. Prior to the measurements, the samples were first outgassed at 300 °C for 3 h under vacuum. SSAs were determined according to the BET (Brunauer–Emmett–Teller) method. Pore-size distributions were calculated by the BJH (Barrett–Joyner–Halenda) method on the desorption branch of the isotherms.

The particle-size distribution was determined using laser diffraction granulometry (MALVERN MS3000). The particles were dispersed in ethanol with an ultrasonic treatment.

Scanning electron microscopy (SEM) micrographs were obtained on a ZEISS SUPRA-55 VP FEG microscope (Oberkochen, Germany). X-ray mappings were obtained from the EDX analyzer OXFORD X-Max 80 (Oxfordshire, United Kingdom) integrated on the same microscope. Images were collected with a voltage of 20 kV.

DRIFT spectroscopy was used to elucidate the sulfation phenomena on the SO₂ powder trap. These measurements were carried out in a Thermo Scientific Nicolet iS50 spectrometer using a praying-mantis accessory (HARRICK high temperature reaction chamber) and a liquid-N₂-cooled MCT detector with a resolution of 2 cm⁻¹. The spectra were recorded from 1000 to 4000 cm⁻¹. The background spectrum was collected on pure and dry KBr. DRIFTS spectra were collected on fresh and sulfated SO₂ traps (i.e., traps that had been exposed to multiple NO-SO₂ cycles) at 35, 200 and 500 °C under 50 mL/min of He. The reported spectra are the result of subtracting from the sulfated-trap spectra measured at each temperature that of the non-sulfated-trap (fresh adsorbent) used as a reference and also collected under He at the corresponding temperature. Finally, to verify the protection effect of the SO₂ trap on the NO_x sensor, the DRIFTS spectra of the SO₂-poisoned sensor and the protected sensor were recorded at room temperature. The latter sensor is supposed to be protected by a SO₂ trap. Note that the sensor was adapted to the reaction chamber of the DRIFT cell to favor the measurements directly on the sensor surface.

Thermogravimetric (TGA) analyses of sulfated trap were performed with a TGA Mettler-Toledo analyzer. The data were obtained in 1 L/h of air, from room temperature to 1300 °C, with a temperature ramp of 10 °C/min.

2.3. SO₂ Adsorption and Regeneration Experiments

The SO₂ adsorption capacity was investigated by cyclic adsorption and regeneration experiments in a fixed-bed reactor. Samples were introduced in a vertical U-shaped quartz reactor (12 mm inner diameter) fitted with a fritted quartz layer. Before the SO₂ adsorption step, the adsorbent was heated at 500 °C (ramp of 10 °C/min from room temperature) under 20 vol.%O₂/He for 1 h to eliminate surface impurities and the humidity. The adsorption experiments were performed at 500 °C for 1 h, using a gas mixture containing 75 ppm of SO₂, 0.9 vol.% of O₂ and 2 vol. % of H₂O, balanced with He, to mimic the conditions encountered in a glass-melting furnace exhaust. The gas flow rate was fixed at 30 L/h and adjusted by BROOKS 5850 mass flow controllers. On-line SO₂ analysis was continuously performed by a multi-gas FTIR analyzer (MKS 2030). The regeneration steps were performed right after the adsorption step, in the same experimental setup, during temperature-programmed desorption (TPD) experiments in He. TPD was performed from 500 to 700 °C at 10 °C/min in a He flow of 30 L/h, and the temperature was maintained at 700 °C for 15 min. After each cycle, the sample was cooled down to 500 °C in 20 vol.%O₂/He to re-oxidize the Cu species.

The SO₂ adsorption capacity of the adsorbent ($C_{\text{ads}}^{\text{TPD}}$ expressed in moles of adsorbed SO₂ per gram of adsorbent) was calculated by the integration of the TPD spectra, according to Equation (1):

$$C_{\text{ads}}^{\text{TPD}} = \frac{F_g \int_{t_0}^{t_f} C dt}{10^6 V_m m_{\text{ads}}} \quad (1)$$

where F_g is the gas flow rate (in L/h); C is the SO₂ outlet concentration (in ppm); t_0 and t_f (in h) are, respectively, the starting and the ending time of the regeneration step; V_m is the molar volume (24.5 L/mol at 25 °C and 1 atmosphere) and m_{ads} is the mass of adsorbent (in g). All the SO₂ adsorption–regeneration tests were performed using an adsorbent mass of 0.1 g. These adsorption–regeneration (TPD) cycles were repeated 3 times for each SO₂ trap.

2.4. Experimental Setup for NO_x Sensor Studies

The electrochemical planar sensor, which was composed of a YSZ porous layer and three metallic electrodes (Pt-Au-Pt), was elaborated by screen-printing (R23-Meteor 23'' semi-automatic screen-printer) on alumina substrates (2 cm × 5 cm), as described by Nematbakhsh et al. [57]. The electrolyte layer of YSZ (home-made ink) was first screen-printed and sintered at 1380 °C for 2 h. The electrodes were printed on a YSZ layer using commercial inks of Pt and Au, followed by 1 h sintering at 850 °C. A Pt heater was also printed on the reverse side of the alumina support to control the sensor temperature. The connectors, welding areas and protector dielectric film were deposited on both sides of the sensor. A catalytic-filter layer consisting of Pt (5 wt.%Pt, MERCK) dispersed in alumina was deposited over the sensing elements with a subsequent calcination process at 850 °C for 1 h. A schematic figure of the fabricated sensors is shown in Figure 1.

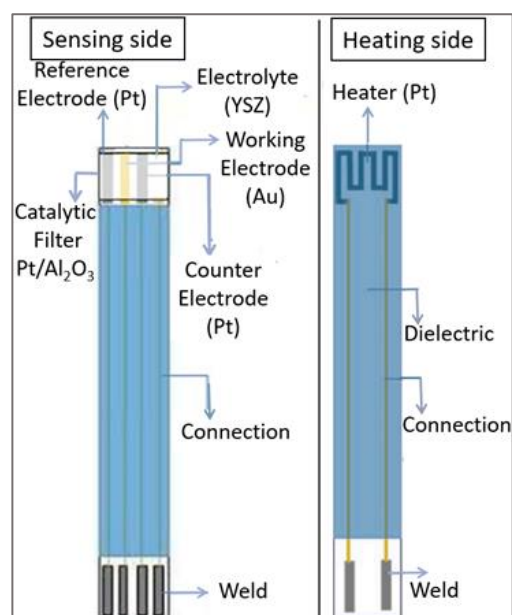


Figure 1. Scheme of the fabricated three-electrode sensor (Pt-Au-Pt) equipped with a catalytic filter (Pt/Al₂O₃).

A measurement bench fully described by Nematbakhsh et al. [57] was used to study the responses of two sensors operating simultaneously in two separated cells. A polarization current of 50 nA was applied between the negatively polarized Au working electrode (WE) and the Pt counter-electrode (CE) to induce electrochemical reductions at the Au/YSZ interface. The sensor response (ΔV_{RE}) was measured between the Pt reference electrode (RE) and WE. The responses to NO₂, NO and SO₂ in respective amounts of 100, 100 and 40 ppm were recorded at 510 °C in a base gas composed of 5 vol.% O₂ and 1.5 vol.% H₂O, balanced with N₂. The total flow rate was fixed at 60 L/h, corresponding to 30 L/h per cell. The gas flow, regulated by mass flow controllers, passed first into a mixing chamber before being sent to the sensor cell.

To study the ability of the prepared SO₂ traps to protect the NO_x sensor from sulfur poisoning, a “SO₂ trap system” was integrated into the test bench and located upstream of the NO_x sensor cell to adsorb the SO₂ before it reaches the sensor. This system mainly consisted of a tubular furnace equipped with a vertical quartz flow-through reactor inside. The trap material was heated to 500 °C, as during the SO₂ adsorption capacity tests. In this fixed-bed reactor, the used amount of each adsorbent was selected to optimize the adsorption capacity while maintaining a uniform gas flow without any pressure drop caused by the catalytic bed. According to the different particle arrangements in the reactor, catalyst weights were 0.8 g and 1.5 g for 6.5%CuO/5%BaO/SBA-15 and 6.5%CuO/24.5%BaO/SBA-15 traps, respectively. To assess the adsorption capacity of the SO₂ traps and understand

the sensors' responses, FTIR gas analyzer (Gaset DX 4015) was placed at the exits of the sensor cells for analyzing the SO₂, NO and NO₂ gases.

3. Results and Discussion

3.1. Physico-Chemical Characterizations of 6.5%CuO/5%BaO/SBA-15 and 6.5%CuO/24.5%BaO/SBA-15 Traps

Table 1 summarizes the chemical compositions, textural properties (determined from N₂ physisorption) and particle sizes of the SBA-15 mesoporous silica calcined at 900 °C and of the two SO₂ traps.

Table 1. Chemical compositions, textural properties and particle sizes of the SBA-15-based adsorbents.

Sample	SBA-15 ^a	6.5%CuO/5%BaO/SBA-15	6.5%CuO/24.5%BaO/SBA-15
CuO content (wt.%) ^b	-	6.6	6.0
BaO content (wt.%) ^b	-	4.8	22.3
SSA (m ² /g)	406	235	132
Total pore volume (cm ³ /g)	0.95	0.42	0.22
Pore size (nm)	6.5	4	4
D50 (μm) ^c	27	19	11

^a Calcined at 900 °C; ^b Determined by ICP analysis. The relative uncertainty is estimated to 0.1%; ^c Median particle size as determined by laser diffraction granulometry.

The actual percentages of CuO and BaO were in agreement with the theoretical ones (values reported in the sample nomenclatures), indicating that the synthesis method was appropriate. It is noteworthy that the small differences between these values could be considered acceptable, given the mass (5 g) of each prepared batch of the two adsorbents.

Figure 2 reports the low-angle XRD patterns of the SBA-15 support as well as the CuO/BaO/SBA-15 adsorbents. For SBA-15 support, the main reflections were located at $2\theta = 1^\circ, 1.8^\circ, 2.1^\circ$ and 2.8° , which correspond to the reflection planes (100), (110), (200) and (210). These planes confirm the ordered hexagonal mesoporous structure of SBA-15 with P6mm symmetry [58].

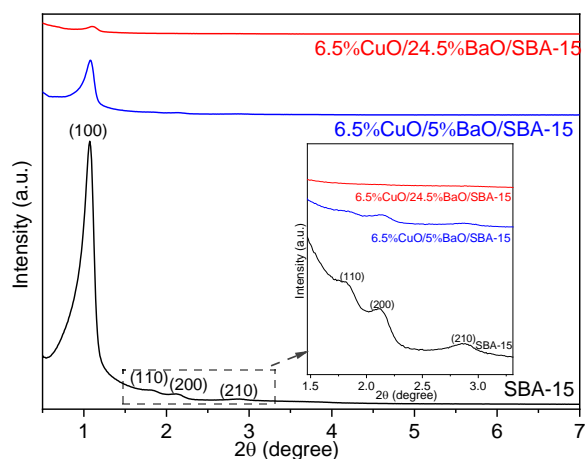


Figure 2. Low-angle XRD patterns of SBA-15 support (calcined at 900 °C) and CuO/BaO/SBA-15 adsorbents. For a better visibility, the diffraction patterns are shifted along the Y-axis. The insert corresponds to a zoom between $2\theta = 1.5^\circ$ and $2\theta = 3.3^\circ$.

For both adsorbents, however, the intensity of the (100) reflection was strongly reduced, and the other reflections were not clearly observed, suggesting a loss in the crystallographic order of the mesoporous structure. Similar results were presented by Mathieu et al. [59], suggesting the formation of CuO and BaO metal oxides inside the mesopores of SBA-15

support after the calcination step. It must be emphasized that the diffraction peak (100) shows a slight shift towards higher angles, which is characteristic of a smaller lattice parameter and can probably be attributed to the successive calcination steps after the addition of both active phases [59].

The corresponding wide-angle XRD patterns are reported in Figure 3. As expected, the SBA-15 support shows a very wide diffraction peak at $2\theta = 20\text{--}30^\circ$ without any other peaks, confirming its amorphous structure. After the addition of CuO and BaO, the XRD patterns of both adsorbents reveal the presence of crystalline CuO phase, suggesting the presence of large CuO nanoparticles after the calcination at 600°C [48]. Moreover, for 6.5%CuO/24.5%BaO/SBA adsorbent, clear diffraction peaks corresponding to barium carbonate (BaCO_3) formed in ambient air and barium silicate (Ba_2SiO_4) were detected. A high BaO loading seems to favor the solid-state reaction between BaO and the SBA support to form Ba_2SiO_4 . This phase and Ba carbonate were not observed on the diffractogram of 6.5%CuO/5%BaO/SBA, most likely due to its lower Ba loading.

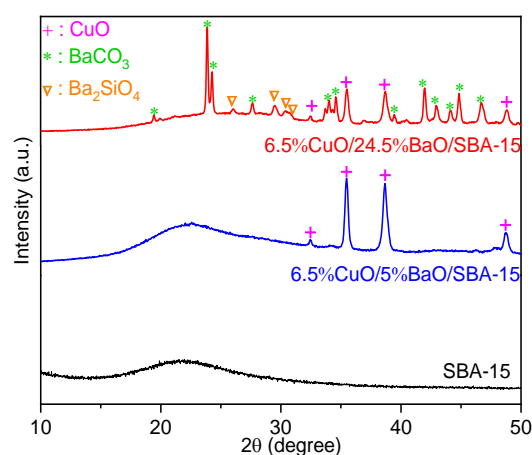


Figure 3. Wide-angle XRD patterns of SBA-15 support (calcined at 900°C) and CuO/BaO/SBA-15 adsorbents. For a better visibility, the diffraction patterns are shifted along the Y-axis.

The N_2 physisorption isotherms and the corresponding BJH pore-size distributions of the SBA-15 support and the CuO/BaO/SBA-15 adsorbents are reported in Figure 4, and their textural properties are presented in Table 1. The SBA-15 support displays a type IV isotherm defined by parallel adsorption and desorption branches with a type H1 hysteresis loop in the relative pressure range $P/P_0 = 0.7\text{--}0.9$. These profiles are characteristic of organized mesoporous materials with well-ordered cylindrical pores, according to the IUPAC classification [60]. However, for both CuO/BaO/SBA-15 adsorbents, the shape of the isotherm was modified, and the hysteresis showed a shift toward lower relative pressures. According to Berger et al. [61], this shift is probably due to the partial plugging of the pores with copper- or barium-based phases, in good agreement with wide-angle XRD patterns (Figure 3).

Moreover, the capillary condensation of both adsorbents is less steep, revealing a decrease in pore size (average pore sizes were 6.5 nm for SBA-15 and 4 nm for both adsorbents), as shown by Gaudin et al. [48]. The addition of CuO and BaO clearly affects the pore volume of the SBA-15 support, which decreases from $0.95\text{ cm}^3/\text{g}$ for the support to 0.42 and $0.22\text{ cm}^3/\text{g}$ for 6.5%CuO/5%BaO/SBA-15 and 6.5%CuO/24.5%BaO/SBA-15 adsorbents, respectively (Table 1). The same trend is also observed in SSAs, which decrease from $406\text{ m}^2/\text{g}$ to $235\text{ m}^2/\text{g}$ and $132\text{ m}^2/\text{g}$, respectively. These modifications in textural properties might be due to the blockage of the mesoporous support after the incorporation of the CuO and BaO active phases [49]. This effect is, as expected, more pronounced with a higher BaO loading.

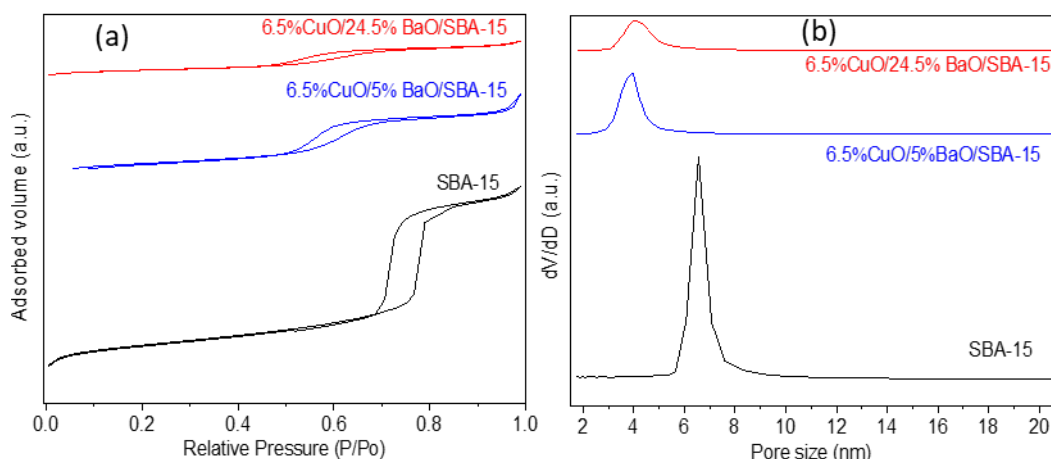


Figure 4. N_2 physisorption isotherms (a) and the corresponding BJH pore-size distributions (b) of SBA-15 support (calcined at $900\text{ }^\circ\text{C}$) and CuO/BaO/SBA-15 adsorbents. For better visibility, the curves are shifted along the Y-axis.

Figure 5 illustrates the particle-size distributions of SBA-15 and CuO/BaO/SBA-15 adsorbents, while Table 1 summarizes their median diameters (D_{50}). The SBA-15 support calcined at $900\text{ }^\circ\text{C}$ shows a unimodal size distribution with a median diameter D_{50} of $27\text{ }\mu\text{m}$. However, a small bump is observed for diameters larger than $58\text{ }\mu\text{m}$, which is probably due to particles being strongly agglomerated. After the incorporation of CuO and BaO, both adsorbents show a shift of particle-size distribution toward lower diameters.

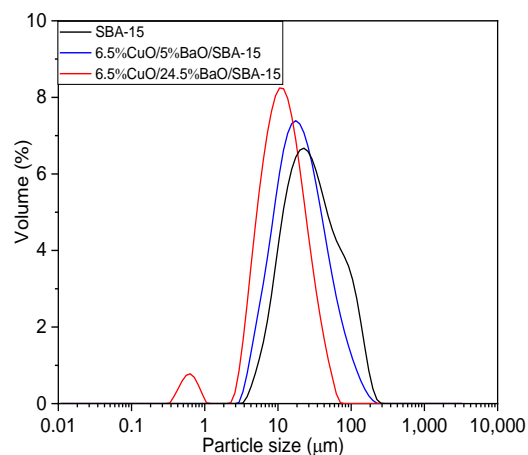


Figure 5. Particle-size distribution of SBA-15 support (calcined at $900\text{ }^\circ\text{C}$) and CuO/BaO/SBA-15 adsorbents, obtained by laser granulometry.

The median diameters D_{50} are $19\text{ }\mu\text{m}$ and $11\text{ }\mu\text{m}$ for $6.5\%\text{CuO}/5\%\text{BaO}/\text{SBA-15}$ and $6.5\%\text{CuO}/24.5\%\text{BaO}/\text{SBA-15}$, respectively. This reduction in particle size after impregnation can be explained by the formation of small copper- or barium-based particles during the synthesis process. These particles can be detached from the support, leading to the decrease in the overall median diameter. Additionally, the metal oxide particles can diffuse into the pores of the SBA-15 support, leading to the formation of smaller particles due to confinement effects. Hence, these effects are more pronounced for the $6.5\%\text{CuO}/24.5\%\text{BaO}/\text{SBA-15}$ adsorbent with a higher BaO loading, which shows a lower median diameter. It is noteworthy that the $6.5\%\text{CuO}/5\%\text{BaO}/\text{SBA-15}$ adsorbent presents a unimodal size distribution, as does the SBA-15 support, while the $6.5\%\text{CuO}/24.5\%\text{BaO}/\text{SBA-15}$ displays a small peak, at less than $1\text{ }\mu\text{m}$, which could indicate the presence of a population of BaCO_3 agglomerates.

The SEM micrographs and the corresponding X-ray mappings of adsorbents are shown in Figure 6. As expected from XRD results (Figure 3), the Cu-X-ray mappings of both adsorbents (Figure 6c,d) reveal the presence of large CuO agglomerates in the range of 2–3 μm that were also visible on the corresponding micrographs (Figure 6a,b), but a greater proportion of copper remains homogeneously distributed on the support. However, the Ba-X-ray mapping of the 6.5%CuO/5%BaO/SBA-15 adsorbent (Figure 6e) displays a homogeneous distribution of barium-based particles, whereas the 6.5%CuO/24.5%BaO/SBA-15 adsorbent (Figure 6f) shows relatively large micrometric agglomerates in the range of 5–10 μm . These results fit well with the XRD patterns (Figure 3), which exhibit strong BaCO₃ and Ba₂SiO₄ peaks only for the 6.5%CuO/24.5%BaO/SBA-15 adsorbent with a higher BaO loading.

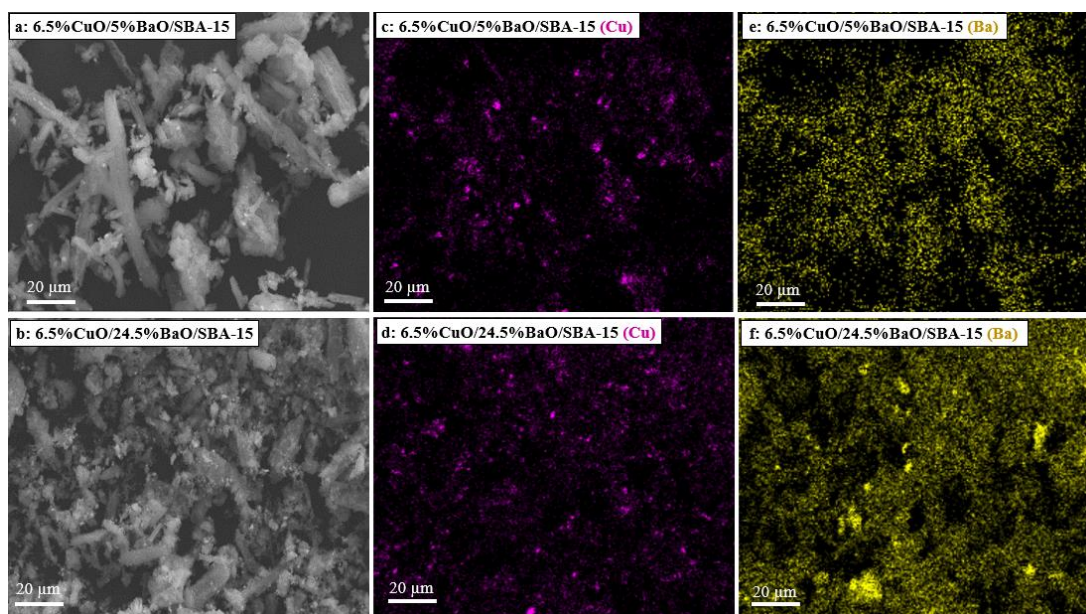


Figure 6. SEM micrographs (a,b) and corresponding X-ray mappings of copper (c,d) and barium (e,f) of 6.5%CuO/5%BaO/SBA-15 and 6.5%CuO/24.5%BaO/SBA-15 adsorbents, respectively.

3.2. SO₂ Adsorption Capacity Measurements

The CuO/BaO/SBA-15 adsorbents were subjected to successive SO₂ adsorption–regeneration cycles in a fixed-bed reactor, as mentioned in the experimental design section. The SO₂ breakthrough curves and TPD spectra obtained during multicycle experiments are reported in Figures 7 and 8, respectively. The SO₂ adsorption capacities, expressed in $\mu\text{molSO}_2/\text{g}_{\text{ads}}$, are presented in Table 2.

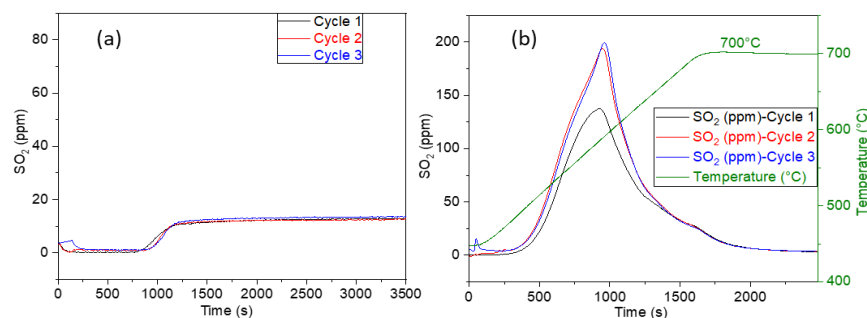


Figure 7. SO₂ breakthrough (a) and TPD (b) curves of the 6.5%CuO/5%BaO/SBA-15 adsorbent submitted to three adsorption (75 ppm SO₂, 0.9 vol.% O₂, 2 vol.% H₂O, balance He, 500 °C, 30 L/h) and regeneration (He, 700 °C, 30 L/h) cycles.

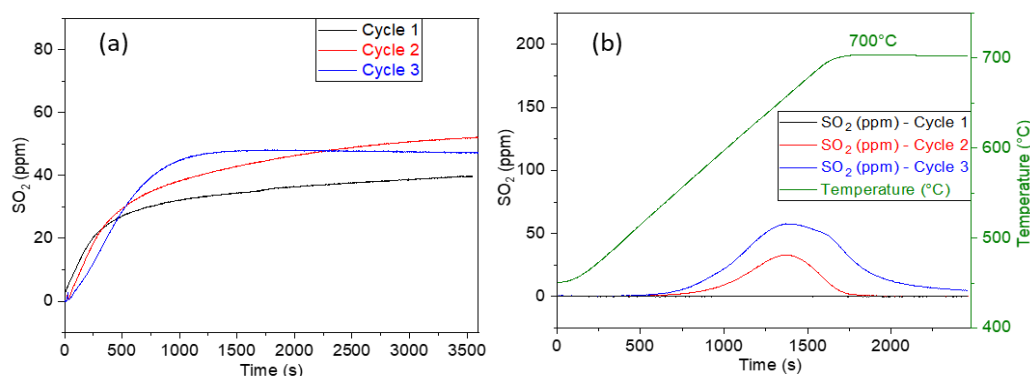


Figure 8. SO₂ breakthrough (a) and TPD (b) curves of the 6.5%CuO/24.5%BaO/SBA-15 adsorbent submitted to three adsorption (75 ppm SO₂, 0.9 vol.% O₂, 2 vol.% H₂O, balance He, 500 °C, 30 L/h) and regeneration (He, 700 °C, 30 L/h) cycles.

Table 2. SO₂ adsorption capacity expressed per g of adsorbent of the 6.5%CuO/5%BaO/SBA-15 and 6.5%CuO/24.5%BaO/SBA-15 traps along three adsorption–regeneration cycles.

Adsorbent	SO ₂ Adsorption Capacity (C _{ads} ^{TPD}) ^a (μmolSO ₂ /g _{ads})		
	Cycle 1	Cycle 2	Cycle 3
6.5%CuO/5%BaO/SBA-15	312	398	395
6.5%CuO/24.5%BaO/SBA-15	-	44	121

^a Calculated from the integration of the TPD curves.

For the first cycle, the 6.5%CuO/5%BaO/SBA-15 adsorbent shows a breakthrough at 15 min (Figure 7a) followed by an increase of the SO₂ outlet concentration up to 13 ppm when 75 ppm of SO₂ are injected for 1 h. This suggests that a fraction of SO₂ is still adsorbed, and the saturation of the adsorbent surface has not been reached after 1 h on-stream. After the second and the third adsorption–regeneration cycles, similar shapes of the breakthrough curves were obtained, which indicates a good stability of the adsorbent with a great reproducibility of the adsorption step over cycles. From TPD curves (Figure 7b), the regeneration peaks occur at around 580 °C, which corresponds to the decomposition of copper sulfates, as described in the literature [48] and according with a previous test of a sulfated adsorbent containing only copper that showed a similar regeneration peak. The SO₂ adsorption capacity, calculated by the integration of TPD curves (Figure 7b, Table 2), increases after the first cycle, from 312 up to around 400 μmolSO₂/g_{ads}, as confirmed by TPD curves (Figure 7b). As shown by Berger et al. [62], such a behavior could probably be assigned to some beneficial changes in the adsorbent porosity along the cycles, which would enable access to additional copper-based active sites.

The increase in the BaO loading modifies the SO₂ adsorption properties (Figure 8a). No complete SO₂ uptake was observed for the 6.5%CuO/24.5%BaO/SBA-15 over its cycles. After 1 h of sulfation under 75 ppm of SO₂, the outlet concentration was around 40–50 ppm for the three cycles. The absence of a total SO₂ adsorption period may be due to the gas flow having bypassed the adsorbent bed through preferential paths, as the bed height is 6 mm, and/or to possible intra-granular diffusional limitations which would have prevented the gas from accessing the pores of small grains. This phenomenon could limit the interaction between SO₂ and the adsorbent, ultimately reducing the adsorption efficiency. In addition, the TPD curves of the first cycle (Figure 8b) do not show any desorption of SO₂, suggesting that sulfates formed during the first adsorption step are stable in He up to 700 °C. Despite the non-regeneration of the trap during the first TPD, the adsorbent continues to store SO₂ during the second adsorption step at 500 °C while the second TPD shows a small SO₂ desorption peak that further increases during the third TPD. This observation might be explained by the sulfation of some active sites that were bypassed by SO₂ and therefore

not sulfated during the first cycle. It should be noted that the regeneration peaks of this adsorbent occur at around 660 °C, whereas the other adsorbent, with lower BaO loading, shows desorption peaks at 580 °C (Figure 7b), which indicates the formation of different types of sulfates species. The SO₂ storage capacity during the first several minutes increases with the number of cycles, suggesting an increase of the porosity of the adsorbent over cycles, limiting the intra-granular diffusional limitations.

As a partial conclusion, the 6.5%CuO/5%BaO/SBA-15 is more efficient than the 6.5%CuO/24.5%BaO/SBA-15 adsorbent for the adsorption of SO₂. With the hypothesis that both adsorbents present the same CuO dispersion, the limited performance of the 6.5%CuO/24.5%BaO/SBA-15 adsorbent is probably related to a negative impact caused by the higher BaO loading. One possible explanation might be the formation of large barium-based particles, which have been previously identified by XRD and are visible by SEM-X-ray mapping analyses. In agreement with the findings of Centi et al. [38], the sulfation of such particles is a limiting process due to the slow bulk diffusion of SO₂ molecules. Furthermore, as clearly highlighted by the N₂ physisorption isotherms, these particles may cause a pore-blocking phenomenon, limiting the ability of SO₂ to access active sites. It is also possible that during the second impregnation step, the higher BaO loading (24.5 wt.% vs. 5 wt.%) could have led to more blockage of the CuO sites, resulting in a significant reduction in the total number of accessible sites.

3.3. NO_x Sensors' Responses

As mentioned in the experimental section, a three-electrode NO_x sensor (Pt-Au-Pt) equipped with a catalytic filter (Pt/Al₂O₃) was tested at 510 °C, with a polarization current of 50 nA between the Au working electrode and the Pt counter electrode. The sensor signal measurements were performed on an electronic card used to make galvanostatic measurements of the sensors, as described by Nematbakhsh et al. [57]. The galvanostat used allowed monitoring of the polarization current and the measurement of the potential between the working and reference electrodes.

To evaluate the capacity of the CuO/BaO/SBA-15 traps to protect our NO_x sensor, the responses of this sensor to 100 ppm NO₂, 100 ppm NO, and 40 ppm SO₂ were recorded in the absence, and in the presence, of both SO₂ traps heated to 500 °C (base gas: 5 vol.% O₂, 1.5 vol.% H₂O in N₂). Before the injection of any gas (NO_x or SO₂), the sensor response was stabilized for 2 h on the polarization current.

Figure 9a compares the sensor responses to NO₂ and NO without, and with, a SO₂ trap located upstream, and Figure 9b–d display the corresponding NO_x outlet concentrations. The inlet gas is denoted as “in” and the outlet as “out”. The aim of these measurements is to investigate the interaction of the SO₂ traps with NO_x and the latter's influence on the sensor response. The results in Figure 9a show that the sensor presents negative responses with similar amplitudes to NO₂ and NO in the absence of the SO₂ trap, as expected and reported by Gao et al. [22]. Indeed, when the sensor is equipped with a catalytic filter, the thermodynamic equilibrium of NO/NO₂ is achieved, resulting in a response with the same amplitude and direction for either NO₂ or NO.

Interestingly, the same behavior with very similar responses was obtained in the presence of either 6.5%CuO/5%BaO/SBA-15 or 6.5%CuO/24.5%BaO/SBA-15 traps upstream of the sensor. The slight shift of the response towards lower ΔV_{RE} values observed with the 6.5%CuO/5%BaO/SBA-15 trap may be due to a small difference in the sensor temperature.

To understand the sensor response during these three tests, the NO_x outlet concentrations were analyzed. Without a SO₂ trap (Figure 9b) and for an inlet NO₂ concentration of 100 ppm, the gas analyzer displays a lower NO₂ value (around 85 ppm) and also reveals the presence of NO (around 5 ppm) at the cell exit. Therefore, the total NO_x concentration was 90 ppm for a NO₂ set point of 100 ppm. The same results were reproduced, and may be due to a lower concentration in the NO₂ cylinder or a small deviation of the mass flow controller. This may have no consequence for our results, since the total NO_x concentration

is relatively preserved and constant. For the NO gas, the outlet concentration fits with the set point of 100 ppm. It should be noted that the measured concentrations do not represent those at the sensor surface, where the NO/NO₂ thermodynamic equilibrium should be reached due to the catalytic filter effect.

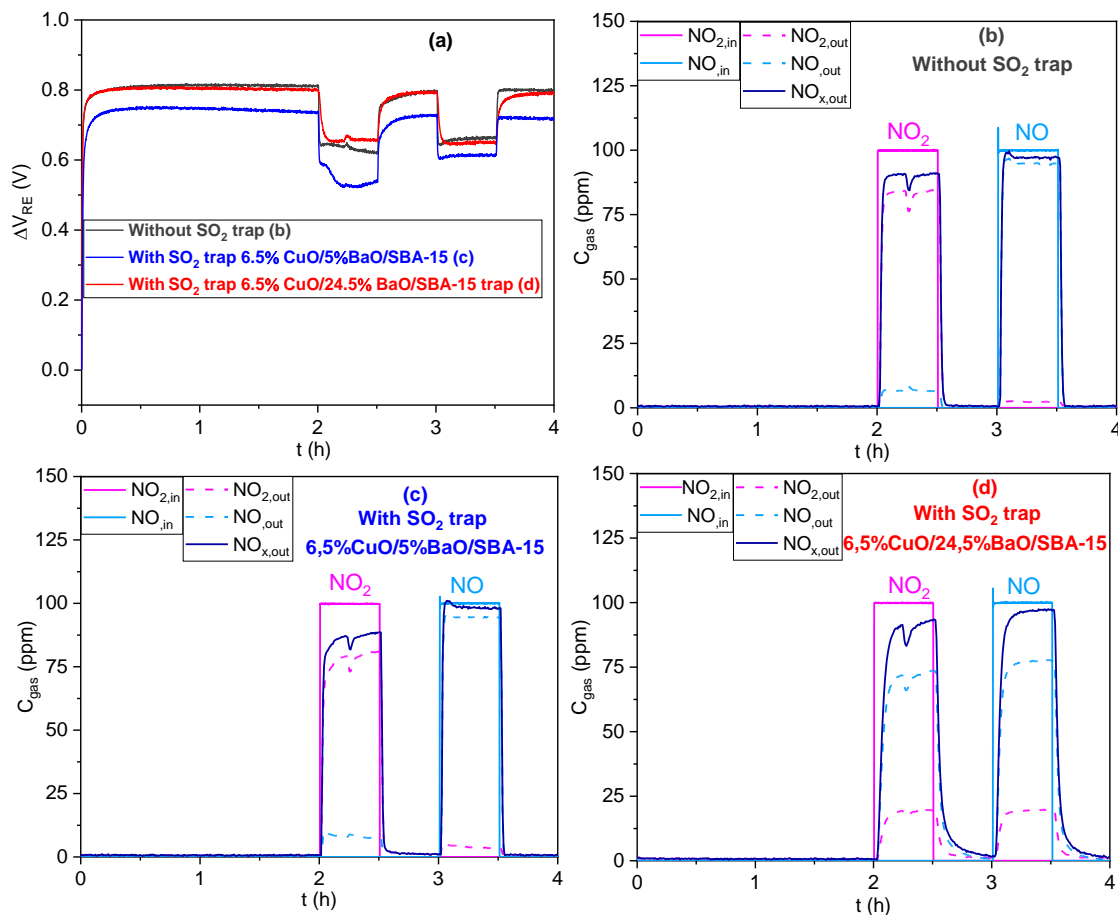


Figure 9. NOx sensor response ($\Delta V_{RE} = f(t)$) to 100 ppm NO₂ and 100 ppm NO (a) and the corresponding gas outlet concentrations ($C_{gas} = f(t)$): (b) without SO₂ trap; (c) with SO₂ trap 6.5%CuO/5%BaO/SBA-15; and (d) with SO₂ trap 6.5%CuO/24.5%BaO/SBA-15. Base gas: 5 vol.% O₂, 1.5 vol.% H₂O in N₂. Solid lines illustrate the concentrations of NO and NO₂ gases sent to the system and dashed lines correspond to gases analyzed at the outlet.

With the 6.5%CuO/5%BaO/SBA-15 trap (Figure 9c), the NOx concentrations at the outlet are very similar to those obtained without the trap (Figure 9b) for both NO₂ and NO exposures. This result indicates that the 6.5%CuO/5%BaO/SBA-15 trap does not seem to significantly adsorb NOx, which is consistent with the specifications. It should be emphasized that the gas flow passes through the SO₂ trap powder bed with a residence time, unlike its subsequent traversal through the catalytic filter of the sensor, which justifies the finding that the trap is the only factor responsible for gas composition variations.

However, the 6.5%CuO/24.5%BaO/SBA-15 trap (Figure 9d) with a higher BaO loading presents an interaction with NO₂ and NO. Indeed, for an inlet NO₂ concentration of 100 ppm, only 20 ppm of NO₂ was detected at the outlet, along with 73 ppm of NO, meaning that this trap can convert NO₂ to NO. Nevertheless, the total NOx concentration remained relatively unchanged, compared to the test without the trap (Figure 9b). For an inlet NO concentration of 100 ppm, a less-pronounced conversion is obtained (78 ppm of NO and 20 ppm of NO₂) and the same NOx concentration was detected at the outlet. Hence, this trap seems to reach the thermodynamic equilibrium NO/NO₂, but without any significant NOx adsorption, since the total NOx concentration is still preserved. As

previously mentioned in the introduction, BaO is known as a primary adsorbent material in NO_x trap systems, with a much better ability to adsorb NO₂ rather than NO [63]. However, according to Hess et al. [64], the adsorption of NO_x on BaO at 500 °C is thermodynamically limited and the resulting nitrates/nitrites species are unstable, which can explain the very low NO_x adsorption observed in our case. It is noteworthy that the mass used for this trap, which contained 24 wt.%BaO, is higher than the other one, which contained 5 wt.%BaO (1.5 g vs. 0.8 g), which could explain its more pronounced interaction with NO_x.

Thus, with 100 ppm of either NO₂ or NO in the inlet gas, similar NO_x outlet concentrations were detected in the presence of both SO₂ traps. This result can explain the similar responses of the NO_x sensor observed in Figure 9a. Indeed, as shown by Gao et al. [22], the ΔV_{RE} value of a sensor equipped with a catalytic filter does not depend on the NO/NO₂ reaching the sensor, but only depends on the total NO_x concentration. It can be concluded that the presence of these traps does not influence the sensor response to NO_x, which fits well with our objective.

To study the impact of SO₂ on the sensors' performance, the latter were successively subjected to 100 ppm of NO and 40 ppm of SO₂ in the absence of a SO₂ trap (Figure 10). As a result, the sensor showed a high and negative response to 40 ppm of SO₂, with an important decrease in the baseline. Subsequently, its response to 100 ppm of NO was significantly reduced compared to that obtained before SO₂ exposure. A negative and large response was observed again after the second SO₂ exposure. Therefore, it can clearly be noticed that this sensor is significantly poisoned by SO₂, becoming almost unable to respond to NO.

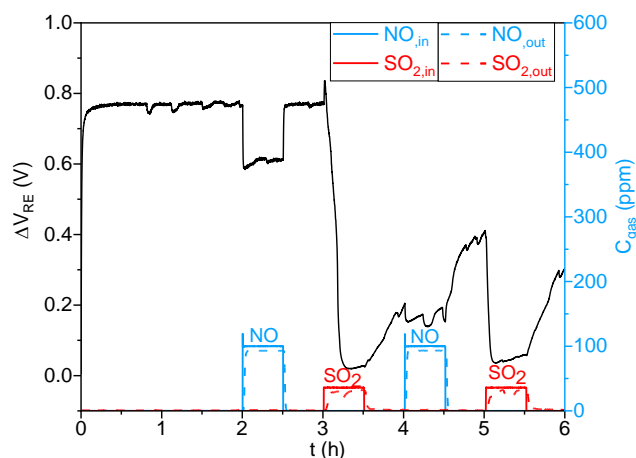


Figure 10. NO_x sensor response (in black) ($\Delta V_{RE} = f(t)$) to 100 ppm NO and 40 ppm SO₂ in the absence of SO₂ trap, with analysis of the gas outlet concentrations ($C_{gas} = f(t)$).

To study the ability of the traps to protect the NO_x sensor from sulfur poisoning, the response of this sensor to 100 ppm of NO and 40 ppm of SO₂ was studied in the presence of the 6.5%CuO/5%BaO/SBA-15 trap (Figure 11) and the 6.5%CuO/24.5%BaO/SBA-15 trap (Figure 12), heated to 500 °C. The sensor was successively exposed to NO and SO₂ until the surfaces of the traps reached saturation. The green lines are used to distinguish tests that were performed separately.

Figure 11 illustrates that during the first NO exposure, the 6.5%CuO/5%BaO/SBA-15 trap converted a fraction of NO to NO₂, which is partially stored, resulting in a total NO_x concentration between 82–90 ppm, instead of 100 ppm of NO in the inlet gas. As expected, the sensor showed a high negative response to the NO_x gases. When exposed to SO₂ for 30 min, the trap allowed a total SO₂ adsorption, with no SO₂ detected at the exit cell, resulting in a total protection of the NO_x sensor from poisoning. Consequently, this trap exhibited a stable response to NO, compared with that obtained before the SO₂ exposure. Until the eighth SO₂ exposure for 30 min, the trap fully stored SO₂ without any SO₂ emissions, and the sensor response to NO was stable and reproducible. However, at

the end of the eighth SO_2 exposure ($t = 23.5$ h), some SO_2 started to pass through the trap, causing the poisoning of the sensor. Therefore, the 6.5%CuO/5%BaO/SBA-15 trap can fully adsorb SO_2 for up to 4 h under the experimental conditions used in this study (flow rate of 60 L/h containing 40 ppm of SO_2 and $m_{\text{ads}} = 0.8$ g).

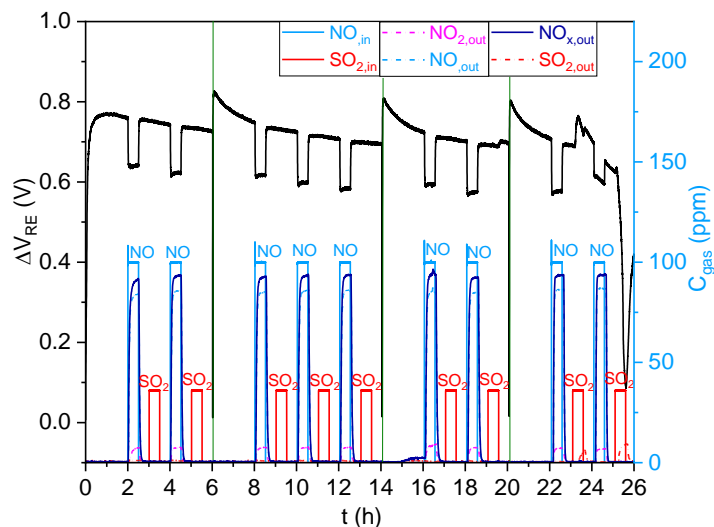


Figure 11. NOx sensor response (in black) ($\Delta V_{\text{RE}} = f(t)$) to 100 ppm NO and 40 ppm SO_2 in the presence of the 6.5%CuO/5%BaO/SBA-15 trap, with analysis of the gas outlet concentrations ($C_{\text{gas}} = f(t)$).

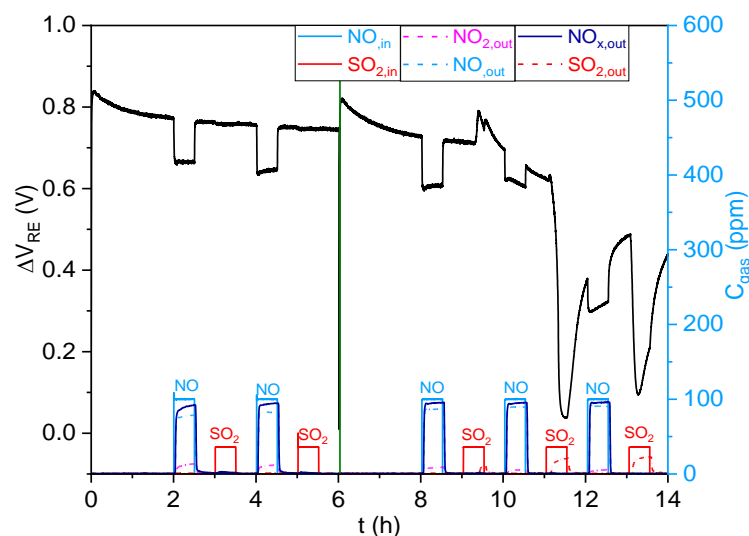


Figure 12. NOx sensor response (in black) ($\Delta V_{\text{RE}} = f(t)$) to 100 ppm NO and 40 ppm SO_2 in the presence of the 6.5%CuO/24.5%BaO/SBA-15 trap, with analysis of the gas outlet concentrations ($C_{\text{gas}} = f(t)$).

The 6.5%CuO/24.5%BaO/SBA-15 trap (Figure 12) exhibited a very low NO adsorption, with a NOx outlet concentration of 90 ppm. This trap allowed a total SO_2 adsorption until the final minutes of the third SO_2 exposure for 30 min, at which point the SO_2 started to be detected at the outlet. At this stage, the sensor showed an unstable response to SO_2 , with a strong change in its baseline. Afterward, the sensor response to NO gradually decreased as the SO_2 outlet concentration increased, until the sensor became almost completely unable to respond to NO. Thus, the 6.5%CuO/24.5%BaO/SBA-15 trap may be able to fully adsorb SO_2 during a total period of 1.5 h (total flow rate of 60 L/h containing 40 ppm of SO_2 and $m_{\text{ads}} = 1.5$ g).

Since the objective is to protect the NO_x sensor from sulfur poisoning, we will only focus on the period of full adsorption of SO₂ by the trap. Therefore, the SO₂ adsorption capacities of both SO₂ traps during the two previous tests (Figures 11 and 12) were calculated based on the period where no SO₂ emission was observed, and were denoted as $C_{\text{ads}}^{\text{Breakthrough}}$. The calculation is performed according to Equation (2):

$$C_{\text{ads}}^{\text{Breakthrough}} = \frac{F_g C_0 t}{10^6 V_m m_{\text{ads}}} \quad (2)$$

where F_g is the gas flow rate (60 L/h), C_0 is the SO₂ inlet concentration (40 ppm), t (in h) is the time period in which no SO₂ emission was observed, V_m is the molar volume (equaling 24.5 L/mol at 25 °C and 1 atmosphere) and m_{ads} is the mass of adsorbent (in g). The calculated adsorption capacities are reported in Table 3.

Table 3. SO₂ adsorption capacities and the corresponding m_{ads} required for 3 months of full SO₂ adsorption under specified conditions, for both CuO/BaO/SBA-15 traps.

Adsorbent	$C_{\text{ads}}^{\text{Breakthrough}}$ ($\mu\text{mol}_{\text{SO}_2}/\text{g}_{\text{ads}}$)	m_{ads} (g) Required for 3 Months of Full SO ₂ Adsorption ^a
6.5%CuO/5%BaO/SBA-15	491	182
6.5%CuO/24.5%BaO/SBA-15	98	912

^a Considering 100 ppm of SO₂ and a total flow rate of 10 L/h.

To meet our industrial requirements, a sufficient amount must be used for the SO₂ trap to fully adsorb SO₂ for 3 months (i.e., 2190 h) and therefore ensure a total protection of the NO_x sensor. The proposed mixture to simulate the adsorption step corresponding to the glass-furnace exhaust contains 100 ppm of SO₂, with a total flow rate of 10 L/h. Based on the SO₂ adsorption capacities $C_{\text{ads}}^{\text{Breakthrough}}$, the mass of each trap required for 3 months of full SO₂ adsorption under the specified conditions was calculated; the results are presented in Table 3.

As shown in Table 3, the 6.5%CuO/5%BaO/SBA-15 trap with the lower BaO loading presents a higher SO₂ adsorption capacity (491 $\mu\text{mol}_{\text{SO}_2}/\text{g}_{\text{ads}}$) than that of the 6.5%CuO/24.5%BaO/SBA-15 trap (98 $\mu\text{mol}_{\text{SO}_2}/\text{g}_{\text{ads}}$), in agreement with previous experiments. Therefore, the estimated mass values required to fully adsorb SO₂ continuously during 3 months under the mentioned specifications are 182 g and 912 g for 6.5%CuO/5%BaO/SBA-15 and 6.5%CuO/24.5%BaO/SBA-15, respectively. It can be concluded that the 6.5%CuO/5%BaO/SBA-15 trap offers the best efficiency and can fully store SO₂ and protect the NO_x sensor for up to 3 months using a mass of 182 g, which appears consistent and feasible at the industrial scale.

3.4. Characterization of the SO₂ Traps and of the NO_x Sensor after Sulfation

In order to highlight the sulfation and its effect on the active phases for SO₂ adsorption, the two traps were characterized by SEM/X-ray mapping (Figures 13 and 14, respectively) after their multiple NO-SO₂ exposures, as reported in Figures 11 and 12.

The SEM micrograph (Figure 13a) and the Cu-X-ray mapping (Figure 13b) of the 6.5%CuO/5%BaO/SBA-15 trap reveal large CuO particles beside smaller ones, while the Ba-X-ray mapping (Figure 13c) shows a homogeneous distribution of Ba-based particles. The same results were observed with the non-sulfated trap (see Figure 6a,c,e) indicating that the sulfation does not significantly affect the dispersion of the active phases within the SBA-15 support. Interestingly, the S-X-ray mapping (Figure 13d) confirms the presence of sulfur species well distributed on the support, most likely copper or/and barium-based sulfates/sulfites. For the 6.5%CuO/24.5%BaO/SBA-15 trap (Figure 14), the distributions of CuO (Figure 14b) and BaO (Figure 14c) seem to be similar to those before sulfation (Figure 6d,f, respectively), since large CuO and BaO particles are still observed. Sulfur-

based species (Figure 14d) are also identified for this type of trap, and probably formed in both CuO and BaO active phases.

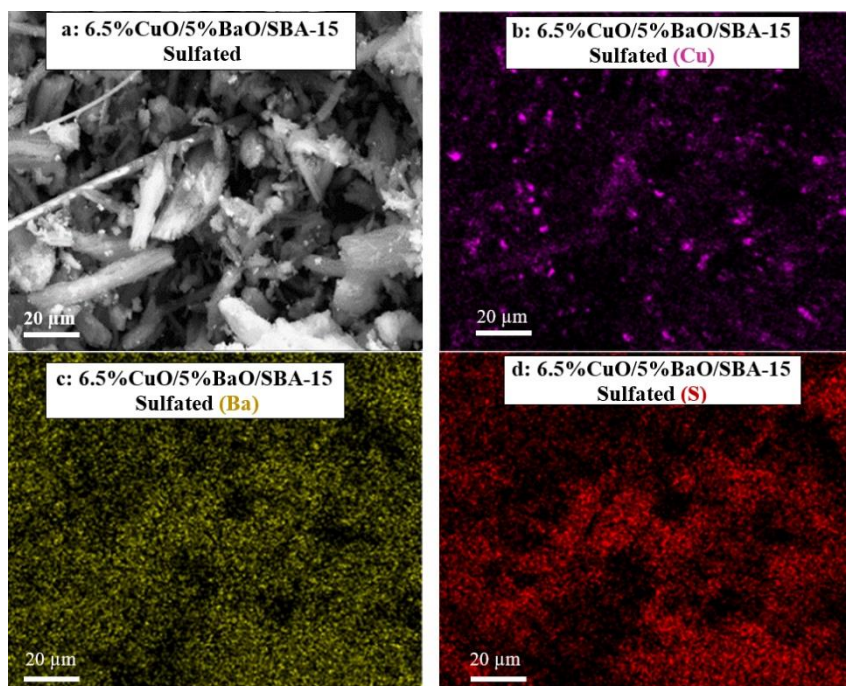


Figure 13. SEM micrograph (a) and X-ray mappings of copper (b), barium (c) and sulfur (d) of the 6.5%CuO/5%BaO/SBA-15 sulfated trap.

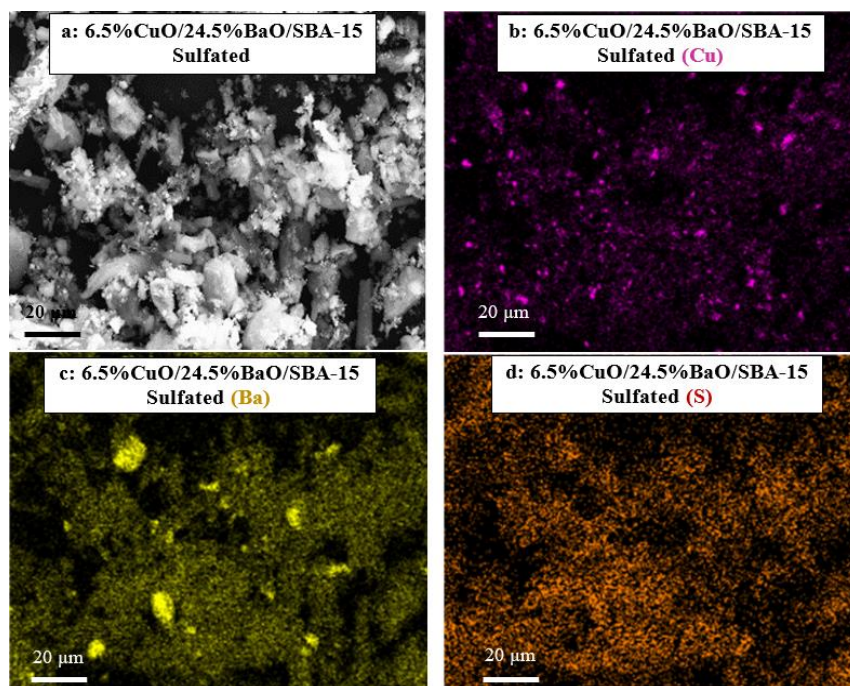


Figure 14. SEM micrograph (a) and X-ray mappings of copper (b), barium (c) and sulfur (d) of the 6.5%CuO/24.5%BaO/SBA-15 sulfated trap.

To identify the SO₂-adsorbed species, the sulfated 6.5%CuO/5%BaO/SBA-15 trap (i.e., after the multiple NO-SO₂ exposures, Figure 11), which is considered the most efficient, was also characterized by DRIFT spectrometry. Moreover, in order to identify in situ the possible regeneration of this trap, a TPD up to 500 °C in He was performed and also was

followed by DRIFTS. Figure 15 shows the DRIFT spectra collected at 35, 200 and 500 °C under 50 mL/min of He. As previously mentioned in the experimental design section, the spectrum of the non-sulfated trap was taken as a reference and subtracted from that of the sulfated sample at the corresponding temperatures.

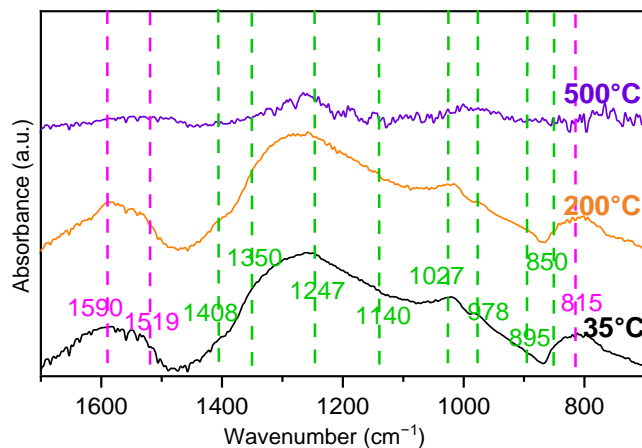


Figure 15. TPD-DRIFTS spectra for sulfated 6.5%CuO/5%BaO/SBA-15 SO₂ trap (after subtracting the non-sulfated trap spectrum) collected at 35, 200 and 500 °C under He. Pink lines = bands associated with nitrates species, and green lines = bands associated with sulfate/sulfites species.

At 35 °C, some broad bands were clearly observed at 978, 1027, 1140 and 1247 cm⁻¹, which can be assigned to the bulk sulfate species adsorbed in BaO [28]. The presence of surface sulfate species was also corroborated by the bands observed in the region of 1340–1400 cm⁻¹ [28,65]. Note that the two shoulders at 850 and 895 cm⁻¹ are attributed to symmetric and asymmetric stretching of monodentate sulfite, respectively [66], suggesting the presence of some sulfites species on the sulfated trap after several cycles of NO-SO₂ exposure. Moreover, in addition to the presence of sulfate/sulfite species, the bands at 815, 1519 and 1590 cm⁻¹ indicate the presence of nitrate species. Indeed, the band at 815 cm⁻¹ is attributed to bridging nitrate [66] or bulk nitrate adsorbed in the BaO phase [67], while the bands at 1519 and 1590 cm⁻¹ are associated with monodentate nitrate [66,68] and chelating bidentate nitrate [67,68], respectively. However, the bands identified in the ranges of 950–1250 cm⁻¹ and 1340–1400 cm⁻¹, which were attributed to sulfates species, could be associated with some nitrates species (bands of surface nitrate species at 1000–1050 cm⁻¹ and 1340–1410 cm⁻¹ [66,67]).

Therefore, it can be concluded that sulfates/sulfites species were formed during the sulfation of the 6.5%CuO/5%BaO/SBA-15 trap, as pointed out by these DRIFTS measurements. Moreover, these sulfates/sulfites species seem to be predominant on the trap surface, compared to nitrates, which suggests a limited adsorption of NO on the trap. However, the formation of some nitrate species, most likely on BaO sites, cannot be excluded.

At 200 °C, no significant changes in the spectrum were observed (Figure 15), suggesting that the adsorbed species are stable at this temperature. With the increase in the temperature to 500 °C, almost all the previously described bands disappeared, indicating that a non-negligible part of the adsorbed species was desorbed at this temperature. However, some small bands attributed to bulk sulfates species adsorbed on BaO sites were still present (978 and 1247 cm⁻¹) suggesting that such species are stable at 500 °C. As reported by Mahzoul et al. [28], the decomposition of barium sulfates can occur at temperatures close to 1000 °C. Furthermore, a broad band in the region 1500–1600 cm⁻¹ can be also observed, which corresponds to some nitrates that were not decomposed at 500 °C. Similar results have been reported in the literature [67,69], showing that nitrates species mainly decompose above 350 °C, but some of them may remain stable even at 500 °C.

Based on these TPD-DRIFTS results, it can be concluded that the regeneration of this sulfated trap at 500 °C in He seems incomplete since some sulfates species are still present

at this temperature. Thus, a higher temperature is required to completely regenerate this trap.

Finally, to confirm the protection of the NO_x sensor from sulfur poisoning in the presence of the 6.5%CuO/5%BaO/SBA-15 trap, the DRIFTS spectra of a sensor that was poisoned by SO₂ was compared to one that was supposed to be protected by a SO₂ trap (Figure 16). Indeed, the poisoned sensor is the one used in the test presented in Figure 11. This sensor was subjected to multiple NO-SO₂ exposures in the presence of the 6.5%CuO/5%BaO/SBA-15 trap before being poisoned by SO₂ not adsorbed by the trap. On the other hand, the so-called protected sensor was exposed for 30 min to NO and 30 min to SO₂ in the presence of the 6.5%CuO/5%BaO/SBA-15 trap, which showed a total SO₂ adsorption. As an assumption, this sensor is supposed to be fully protected from any sulfur poisoning, which will be identified by these DRIFTS experiments (Figure 16). As previously mentioned in the experimental design section, it is important to note that the IR radiation was focused on the sensing side of the sensor covered by the Pt/Al₂O₃ catalytic filter, and the spectra were collected at room temperature. The spectrum of a fresh sensor was taken as a reference and subtracted from those of the poisoned and protected sensors.

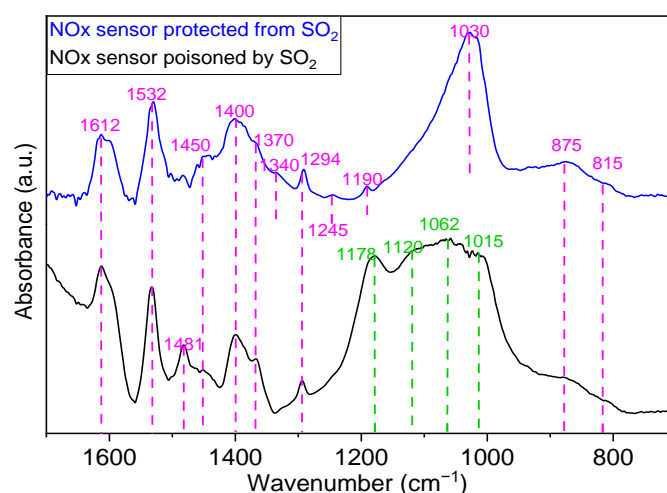


Figure 16. DRIFTS spectra of both the NO_x sensor poisoned by SO₂ and the NO_x sensor protected from SO₂, collected at room temperature. Pink lines = bands associated with nitrates/nitrites species, and green lines = bands associated with sulfates species.

As shown in Figure 16, several bands are common for both poisoned and protected sensors. The positions of these bands and their corresponding assignments are as follows: 815 cm⁻¹ and 875 cm⁻¹ for bridging nitrates [66,70], 1294 cm⁻¹ and 1532 cm⁻¹ for monodentate nitrates [66,68,71], 1612 cm⁻¹ for bridging nitrate associated with Pt [68] and 1370, and 1400 and 1450 cm⁻¹ for monodentate nitrite in the region of 1375–1410 cm⁻¹ [72]. However, the poisoned sensor shows an additional band at 1481 cm⁻¹ attributed to monodentate nitrate [71]. In the same way, some other bands attributed to nitrates/nitrites species are clearly observed on the protected sensor: 1190 cm⁻¹ for monodentate nitrite [70]; 1030 and 1245 cm⁻¹ for chelating or bidentate nitrates, respectively [70,72]; and 1340 cm⁻¹ for water-solvated nitrate [66]. The presence of these different nitrates/nitrites species on both poisoned and protected NO_x sensors can be mainly attributed to the adsorption of NO on either Pt- or Al₂O₃-available sites of the catalytic filter. Based on the working principle of the sensor, one can note that NO is not stored by this filter, but rather undergoes an adsorption–desorption equilibrium during the experiment. Moreover, the DRIFT spectrum of the poisoned sensor shows a broad band in the region of 930–1250 cm⁻¹ which can be deconvoluted in four bands at 1015, 1062, 1120 and 1178 cm⁻¹. These bands could be related to bulk sulfates species, which confirms the poisoning of this sensor by SO₂ and explains the degradation of its performance, as previously shown in Figure 11. It is noteworthy that none of these sulfate bands were detected on the protected sensor, confirming

our assumption that the 6.5%CuO/5%BaO/SBA-15 trap was able to fully capture SO₂, providing a total protection of the sensor from poisoning. In addition, it should be noted that the monodentate nitrites species observed at 1370 and 1400 cm⁻¹ on both sensors (1375–1470 cm⁻¹ region [72]) can overlap with surface sulfates species in the region of 1340–1400 cm⁻¹ [65]. As these two bands seem to be more intense in the spectra of the poisoned sensor than the protected one, they could be attributed to surface sulfate species rather than nitrate species. Furthermore, the band at 1015 cm⁻¹ observed on the surface of poisoned sensor and attributed to sulfate species can also overlap with surface nitrate species in the region of 1000–1050 cm⁻¹ [66].

Based on DRIFTS measurements, it can therefore be concluded that surface sulfates/sulfites and nitrates species were formed on SO₂ traps after several cycles of NO-SO₂ exposures, the former being clearly predominant, which suggests a limited adsorption of NO on the trap. A partial regeneration of the adsorbent surface was also pointed out by these experiments. However, the temperature should be increased to ensure full SO₂ trap regeneration. Finally, the protection role of the SO₂ trap for the NO_x sensor was confirmed, showing that most of the species observed on the surface of the protected sensor can be attributed to the N-containing adsorbed species, and without clear evidence of sulfates/sulfites species. These species were, however, clearly present in the DRIFTS spectrum of the poisoned sensor.

Thermal analyses were performed on a sulfated 6.5%CuO/5%BaO/SBA-15 trap to identify the types of SO₂-adsorbed species. This sulfation was performed at 500 °C and under 40 ppm of SO₂ until the breakthrough, in the same base gas of previous tests (5 vol.% O₂, 1.5 vol.% H₂O in N₂). The thermogravimetric (TGA) and derivative thermogravimetric (DTG) curves in the temperature range of 35–1300 °C are shown in Figure 17. A small weight loss is observed below 100 °C, which may correspond to the release of physically adsorbed water. Another weight loss, of about 0.75%, is detected between 230 to 400 °C. It may be due to the decomposition of copper carbonate into CuO, which occurs at temperatures of 230–300 °C, as previously reported by Shaheen et al. [73].

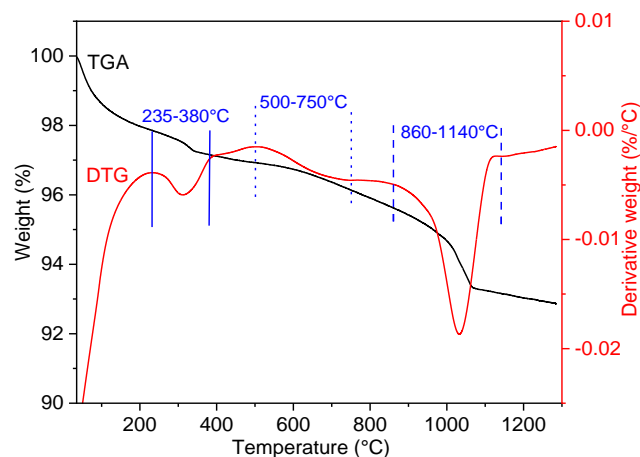


Figure 17. TGA-DTG analyses of the sulfated 6.5%CuO/5%BaO/SBA-15 trap.

However, the main weight loss, of about 2.5%, is observed between 860 and 1140 °C and centered at 1030 °C. This weight loss could be due to the decomposition of barium sulfates or barium carbonates. Since no similar decomposition was observed in the thermal analysis of the fresh trap (results not shown), it can be deduced that this weight loss most likely corresponds to the decomposition of barium sulfates into BaO. Indeed, as shown by Mahzoul et al. [28], the barium sulfate may decompose at 1000 °C. Moreover, Yamazaki et al. [74] showed that such a decomposition could also occur at lower temperatures, around 800 °C, which matches well with our decomposition temperature range. It is important to note that a small weight loss can be observed in the temperature range of 500–750 °C, which may be attributed to the decomposition of copper sulfates to CuO,

as found in the literature [48] and confirmed by our regeneration tests (see Figure 7b). Based on these thermal analysis results, it can be concluded that the barium sites of the 6.5%CuO/5%BaO/SBA-15 trap are probably more active toward SO₂ adsorption than are the copper sites. However, BaO presents a limited catalytic activity for the oxidation of SO₂ to SO₃, which is essential for subsequent adsorption. Therefore, the presence of CuO in the catalyst is necessary to enable this oxidation while giving rise to more adsorption sites.

4. Conclusions

In order to protect the electrochemical NO_x sensor from sulfur poisoning under the glass-furnace exhaust, two different CuO/BaO/SBA-15 adsorbents were synthesized and tested for trapping SO₂ at 500 °C during cyclic adsorption–regeneration experiments. The challenge was to identify a material able to oxidize and trap SO₂, and with a low affinity to NO_x. The whole of the characterizations of these traps shows: (1) the formation of large micrometric CuO particles for both traps, (2) finely dispersed small Ba particles for the 6.5%CuO/5%BaO/SBA-15 and some BaCO₃ micrometric agglomerates on 6.5%CuO/24.5%BaO/SBA-15, and (3) a more pronounced decrease in porous volume, specific surface area and mesoporous organization observed for the 6.5%CuO/24.5%BaO/SBA-15 trap with higher BaO loading.

The SO₂ adsorption–regeneration cycles show that the trap performance strongly depends on the BaO loading. The 6.5%CuO/5%BaO/SBA-15 trap exhibits a better efficiency/stability compromise, with higher adsorption capacity than that of the 6.5%CuO/24.5%BaO/SBA-15 trap after the third cycle.

The NO_x sensor response was studied in the presence of the “SO₂ trap system” placed upstream the sensor. Both traps showed a very low NO_x adsorption and only acted in the NO₂–NO conversion, while preserving the total NO_x concentrations. Therefore, the NO_x sensor response was not impacted by the presence of these traps.

The response of this sensor was investigated during multiple NO–SO₂ exposures in the absence of, and in the presence of, SO₂ traps. In the absence of traps, the sensor was significantly poisoned by SO₂, becoming almost unable to respond to NO. However, in the presence of the 6.5%CuO/5%BaO/SBA-15 trap, a total SO₂ adsorption across 4 h ($m_{\text{ads}} = 0.8$ g) was observed, along with a very low NO adsorption. Consequently, the NO_x sensor was completely protected from SO₂ poisoning and showed a stable response to NO. The 6.5%CuO/24.5%BaO/SBA-15 trap provided a much shorter protection, lasting for only 1.5 h, despite a higher mass ($m_{\text{ads}} = 1.5$ g) implemented. Therefore, the calculated SO₂ adsorption capacity corresponding to the full adsorption of SO₂ ($C_{\text{ads}}^{\text{Breakthrough}}$) was approximately five times higher for the 6.5%CuO/5%BaO/SBA-15 than for 6.5%CuO/24.5%BaO/SBA-15.

In our experimental conditions, a mass of 182 g of the 6.5%CuO/5%BaO/SBA-15 trap would be sufficient to continuously adsorb SO₂ during three months of operation and to protect the NO_x sensor from sulfur poisoning without affecting its response to NO_x. This finding represents a major advance, as previously the main challenge was the interference of NO adsorption with that of SO₂ for copper-based adsorbents. Given the long-term stability of NO_x sensors in harsh environments, which has been previously highlighted in the literature, and with the demonstrated performance of the SO₂ trap throughout the performed tests, it can be concluded that the whole system exhibits robust stability in such challenging conditions.

Finally, the SO₂-adsorbed species on the sulfated traps were successfully identified by SEM-X-ray mapping and DRIFTS measurements. The thermal analysis suggests that SO₂ is predominantly adsorbed on the BaO sites rather than on the CuO sites of the trap.

Future investigation should focus on designing a container for the SO₂ trap and integrating it into industrial setups, upstream of the NO_x sensor in the existing system. This container should present a compacted design that permits the gas to pass through without obstruction while maintaining a sufficient residence time. Such a design

could serve as a unit replaced at regular intervals (e.g., every 3 months) once the catalyst reaches saturation.

Author Contributions: Conceptualization, C.N., M.R., A.B., S.G., P.V. and J.-P.V.; methodology and investigation, C.N., M.R., A.B., S.G., P.V. and J.-P.V.; validation, C.N., M.R., A.B. and S.G.; data curation, C.N., M.R., A.B. and S.G.; writing—original draft preparation, C.N.; writing—review and editing, C.N., M.R., A.B., S.G., P.V. and J.-P.V.; supervision, M.R., A.B., S.G., P.V. and J.-P.V.; funding acquisition, P.V. and J.-P.V. All authors have read and agreed to the published version of the manuscript.

Funding: This research was funded by the Region Auvergne-Rhône-Alpes using the financial resources granted by the Pack Ambition Recherche 2020—Capteur-combustion (CapComb).

Institutional Review Board Statement: Not applicable.

Informed Consent Statement: Not applicable.

Data Availability Statement: The data that support the findings of this study are available from the corresponding author upon reasonable request.

Acknowledgments: The authors would like to acknowledge the Region Auvergne-Rhône-Alpes for funding from the “Pack Ambition Recherche 2020—CapComb”, as well as RB Technologies for its support of this study.

Conflicts of Interest: The authors declare no conflict of interest.

References

1. Liu, T.; Wang, X.; Li, L.; Yu, J. Review—Electrochemical NO_x Gas Sensors Based on Stabilized Zirconia. *J. Electrochem. Soc.* **2017**, *164*, B610–B619. [[CrossRef](#)]
2. Flamme, M. Low NO_x Combustion Technologies for High Temperature Applications. *Energy Convers. Manag.* **2001**, *42*, 1919–1935. [[CrossRef](#)]
3. Yamamoto, H.; Kuroki, T.; Fujishima, H.; Okubo, M. Pilot-Scale NO_x and SO_x Aftertreatment Using a Two-Phase Ozone and Chemical Injection in Glass-Melting-Furnace Exhaust Gas. *IEEE Trans. Ind. Appl.* **2019**, *55*, 6295–6302. [[CrossRef](#)]
4. Yang, B.; Shen, Y.; Shen, S.; Zhu, S. Regeneration of the Deactivated TiO₂-ZrO₂-CeO₂/ATS Catalyst for NH₃-SCR of NO_x in Glass Furnace. *J. Rare Earths* **2013**, *31*, 130–136. [[CrossRef](#)]
5. Wang, D.Y.; Racine, D.M.; Husted, H.; Yao, S. *Sensing Exhaust NO₂ Emissions Using the Mixed Potential Principle*; SAE Technical Paper 2014-01-1487; SAE International: Warrendale, PA, USA, 2014.
6. Gao, J.; Viricelle, J.P.; Pijolat, C.; Breuil, P.; Vernoux, P.; Boreave, A.; Giroir-Fendler, A. Improvement of the NO_x Selectivity for a Planar YSZ Sensor. *Sens. Actuators B Chem.* **2011**, *154*, 106–110. [[CrossRef](#)]
7. Somov, S.; Reinhardt, G.; Guth, U.; Göpel, W. Gas Analysis with Arrays of Solid State Electrochemical Sensors: Implications to Monitor HCs and NO_x in Exhausts. *Sens. Actuators B Chem.* **1996**, *36*, 409–418. [[CrossRef](#)]
8. Zhang, W.F.; Schmidt-Zhang, P.; Guth, U. Electrochemical Studies on Cells M/YSZ/Pt (M=Pt, Pt-Ga₂O₃) in NO, O₂, N₂ Gas Mixtures. *Solid State Ion.* **2004**, *169*, 121–128. [[CrossRef](#)]
9. Yin, C.; Guan, Y.; Zhu, Z.; Liang, X.; Wang, B.; Diao, Q.; Zhang, H.; Ma, J.; Liu, F.; Sun, Y.; et al. Highly Sensitive Mixed-Potential-Type NO₂ Sensor Using Porous Double-Layer YSZ Substrate. *Sens. Actuators B Chem.* **2013**, *183*, 474–477. [[CrossRef](#)]
10. Zosel, J.; Westphal, D.; Jakobs, S.; Müller, R.; Guth, U. Au-Oxide Composites as HC-Sensitive Electrode Material for Mixed Potential Gas Sensors. *Solid State Ion.* **2002**, *152–153*, 525–529. [[CrossRef](#)]
11. Miura, N.; Zhuiykov, S.; Ono, T.; Hasei, M.; Yamazoe, N. Mixed Potential Type Sensor Using Stabilized Zirconia and ZnFe₂O₄ Sensing Electrode for NO_x Detection at High Temperature. *Sens. Actuators B Chem.* **2002**, *83*, 222–229. [[CrossRef](#)]
12. Ferlazzo, A.; Espro, C.; Iannazzo, D.; Bonavita, A.; Neri, G. Yttria-Zirconia Electrochemical Sensor for the Detection of Tyrosine. *Mater. Today Commun.* **2023**, *35*, 106036. [[CrossRef](#)]
13. Ando, B.; Baglio, S.; Castorina, S.; Graziani, S.; Tondepu, S.V.G.; Petralia, S.; Messina, M.A.; Maugeri, L.; Neri, G.; Ferlazzo, A. A Capacitive Sensor, Exploiting a YSZ Functional Layer, for Ammonia Detection. *IEEE Trans. Instrum. Meas.* **2022**, *71*, 1–11. [[CrossRef](#)]
14. Hao, X.; Lu, Q.; Zhang, Y.; Li, W.; Zhang, Y.; Liu, T.; Liang, X.; Liu, F.; Yan, X.; Gao, Y.; et al. Insight into the Effect of the Continuous Testing and Aging on the SO₂ Sensing Characteristics of a YSZ (Yttria-Stabilized Zirconia)-Based Sensor Utilizing ZnGa₂O₄ and Pt Electrodes. *J. Hazard. Mater.* **2020**, *388*, 121772. [[CrossRef](#)]
15. Pasierb, P.; Rekas, M. Solid-State Potentiometric Gas Sensors—Current Status and Future Trends. *J. Solid State Electrochem.* **2009**, *13*, 3–25. [[CrossRef](#)]
16. Zhuiykov, S.; Miura, N. Development of Zirconia-Based Potentiometric NO_x Sensors for Automotive and Energy Industries in the Early 21st Century: What Are the Prospects for Sensors? *Sens. Actuators B Chem.* **2007**, *121*, 639–651. [[CrossRef](#)]

17. Fergus, J.W. Solid Electrolyte Based Sensors for the Measurement of CO and Hydrocarbon Gases. *Sens. Actuators B Chem.* **2007**, *122*, 683–693. [[CrossRef](#)]
18. Guth, U.; Zosel, J. Electrochemical Solid Electrolyte Gas Sensors -Hydrocarbon and NO_x Analysis in Exhaust Gases. *Ionics* **2004**, *10*, 366–377. [[CrossRef](#)]
19. Yang, J.C.; Spirig, J.V.; Karweik, D.; Routbort, J.L.; Singh, D.; Dutta, P.K. Compact Electrochemical Bifunctional NO_x/O₂ Sensor with Metal/Metal Oxide Internal Reference Electrode for High Temperature Applications. *Sens. Actuators B Chem.* **2008**, *131*, 448–454. [[CrossRef](#)]
20. Yang, J.C.; Dutta, P.K. High Temperature Amperometric Total NO_x Sensors with Platinum-Loaded Zeolite Y Electrodes. *Sens. Actuators B Chem.* **2007**, *123*, 929–936. [[CrossRef](#)]
21. Yang, J.C.; Dutta, P.K. High Temperature Potentiometric NO₂ Sensor with Asymmetric Sensing and Reference Pt Electrodes. *Sens. Actuators B Chem.* **2010**, *143*, 459–463. [[CrossRef](#)]
22. Gao, J. Etude et Mise Au Point d'un Capteur de Gaz Pour La Detection Sélective de NO_x En Pot D'échappement Automobile. Ph.D. Thesis, Mines Saint-Etienne, Saint-Étienne, France, 2011.
23. Miura, N.; Lu, G.; Yamazoe, N. High-Temperature Potentiometric/Amperometric NO_x Sensors Combining Stabilized Zirconia with Mixed-Metal Oxide Electrode. *Sens. Actuators B Chem.* **1998**, *52*, 169–178. [[CrossRef](#)]
24. Miura, N.; Lu, G.; Ono, M.; Yamazoe, N. Selective Detection of NO by Using an Amperometric Sensor Based on Stabilized Zirconia and Oxide Electrode. *Solid State Ion.* **1999**, *117*, 283–290. [[CrossRef](#)]
25. Zhuiykov, S.; Nakano, T.; Kunimoto, A.; Yamazoe, N.; Miura, N. Potentiometric NO_x Sensor Based on Stabilized Zirconia and NiCr₂O₄ Sensing Electrode Operating at High Temperatures. *Electrochem. Commun.* **2001**, *3*, 97–101. [[CrossRef](#)]
26. Viricelle, J.P.; Vernoux, P.; Gao, J.; Romanytsia, I.; Breuil, P.; Pijolat, C. NO₂-Selective Electrochemical Sensors for Diesel Exhausts. *Procedia Eng.* **2016**, *168*, 7–10. [[CrossRef](#)]
27. Limousy, L.; Mahzoul, H.; Brilhac, J.F.; Gilot, P.; Garin, F.; Maire, G. SO₂ Sorption on Fresh and Aged SO_x Traps. *Appl. Catal. B Environ.* **2003**, *42*, 237–249. [[CrossRef](#)]
28. Mahzoul, H.; Limousy, L.; Brilhac, J.F.; Gilot, P. Experimental Study of SO₂ Adsorption on Barium-Based NO_x Adsorbers. *J. Anal. Appl. Pyrolysis* **2000**, *56*, 179–193. [[CrossRef](#)]
29. Mathieu, Y.; Tzani, L.; Soulard, M.; Patarin, J.; Vierling, M.; Molière, M. Adsorption of SO_x by Oxide Materials: A Review. *Fuel Process. Technol.* **2013**, *114*, 81–100. [[CrossRef](#)]
30. Bravo, R.V.; Camacho, R.F.; Moya, V.M.; García, L.A.I. Desulphurization of SO₂-N₂ Mixtures by Limestone Slurries. *Chem. Eng. Sci.* **2002**, *57*, 2047–2058. [[CrossRef](#)]
31. Egan, B.Z.; Felker, L.K. Removal of SO₂ from Simulated Flue Gas by Magnesia Spray Absorption: Parameters Affecting Removal Efficiency and Products. *Ind. Eng. Chem. Process Des. Dev.* **1986**, *25*, 558–561. [[CrossRef](#)]
32. Waqif, M.; Saad, A.M.; Bensitel, M.; Bachelier, J.; Saur, O.; Lavalley, J.C. Comparative Study of SO₂ Adsorption on Metal Oxides. *J. Chem. Soc. Faraday Trans.* **1992**, *88*, 2931–2936. [[CrossRef](#)]
33. Marcu, I.C.; Săndulescu, I. Study of Sulfur Dioxide Adsorption on Y Zeolite. *J. Serbian Chem. Soc.* **2004**, *69*, 563–569. [[CrossRef](#)]
34. Zhi, Y.; Zhou, Y.; Su, W.; Sun, Y.; Zhou, L. Selective Adsorption of SO₂ from Flue Gas on Triethanolamine-Modified Large Pore SBA-15. *Ind. Eng. Chem. Res.* **2011**, *50*, 8698–8702. [[CrossRef](#)]
35. Hong, I.; Jiang, H.; Park, Y.D.; Kim, J.Y.; Ha, B.H. Metal Dispersed Activated Carbon Fibers and Their Application for Removal of SO_x. *Chem. Phys. Lett.* **2002**, *366*, 572–577. [[CrossRef](#)]
36. Xie, G.; Liu, Z.; Zhu, Z.; Liu, Q.; Ma, J. Reductive Regeneration of Sulfated CuO/Al₂O₃ Catalyst-Sorbent in Ammonia. *Appl. Catal. B Environ.* **2003**, *45*, 213–221. [[CrossRef](#)]
37. Kikuyama, S.; Miura, A.; Kikuchi, R.; Takeguchi, T.; Eguchi, K. SO_x Sorption-Desorption Characteristics by ZrO₂-Based Mixed Oxides. *Appl. Catal. A Gen.* **2004**, *259*, 191–197. [[CrossRef](#)]
38. Centi, G.; Passarini, N.; Perathoner, S.; Riva, A. Combined DeSO_x/DeNO_x Reactions on a Copper on Alumina Sorbent-Catalyst. 1. Mechanism of SO₂ Oxidation-Adsorption. *Ind. Eng. Chem. Res.* **1992**, *31*, 1947–1955. [[CrossRef](#)]
39. Tseng, H.H.; Wey, M.Y. Study of SO₂ Adsorption and Thermal Regeneration over Activated Carbon-Supported Copper Oxide Catalysts. *Carbon N. Y.* **2004**, *42*, 2269–2278. [[CrossRef](#)]
40. Kiel, J.H.A.; Prins, W.; van Swaaij, W.P.M. Performance of Silica-Supported Copper Oxide Sorbents for SO_x/NO_x-Removal from Flue Gas. I. Sulphur Dioxide Adsorption and Regeneration Kinetics. *Appl. Catal. B Environ.* **1992**, *1*, 13–39. [[CrossRef](#)]
41. Corma, A. From Microporous to Mesoporous Molecular Sieve Materials and Their Use in Catalysis. *Chem. Rev.* **1997**, *97*, 2373–2419. [[CrossRef](#)]
42. Taguchi, A.; Schüth, F. Ordered Mesoporous Materials in Catalysis. *Microporous Mesoporous Mater.* **2005**, *77*, 1–45. [[CrossRef](#)]
43. Gaudin, P.; Michelin, L.; Josien, L.; Nouali, H.; Dorge, S.; Brilhac, J.F.; Fiani, E.; Vierling, M.; Molière, M.; Patarin, J. Highly Dispersed Copper Species Supported on SBA-15 Mesoporous Materials for SO_x Removal: Influence of the CuO Loading and of the Support. *Fuel Process. Technol.* **2016**, *148*, 1–11. [[CrossRef](#)]
44. Gaudin, P.; Dorge, S.; Nouali, H.; Patarin, J.; Brilhac, J.F.; Fiani, E.; Vierling, M.; Molière, M. Synthesis of CuO/SBA-15 Adsorbents for SO_x Removal Applications, Using Different Impregnation Methods. *Comptes Rendus Chim.* **2015**, *18*, 1013–1029. [[CrossRef](#)]
45. Centi, G.; Hodnett, B.K.; Jaeger, P.; Macken, C.; Marella, M.; Tomaselli, M.; Paparatto, G.; Perathoner, S. Development of Copper-on-Alumina Catalytic Materials for the Cleanup of Flue Gas and the Disposal of Diluted Ammonium Sulfate Solutions. *J. Mater. Res.* **1995**, *10*, 553–561. [[CrossRef](#)]

46. Gaudin, P.; Fioux, P.; Dorge, S.; Nouali, H.; Vierling, M.; Fiani, E.; Molière, M.; Brilhac, J.F.; Patarin, J. Formation and Role of Cu⁺ Species on Highly Dispersed CuO/SBA-15 Mesoporous Materials for SO_x Removal: An XPS Study. *Fuel Process. Technol.* **2016**, *153*, 129–136. [[CrossRef](#)]
47. Deng, S.G.; Lin, Y.S. Synthesis, Stability, and Sulfation Properties of Sol-Gel-Derived Regenerative Sorbents for Flue Gas Desulfurization. *Ind. Eng. Chem. Res.* **1996**, *35*, 1429–1437. [[CrossRef](#)]
48. Gaudin, P.; Dorge, S.; Nouali, H.; Vierling, M.; Fiani, E.; Molière, M.; Brilhac, J.F.; Patarin, J. CuO/SBA-15 Materials Synthesized by Solid State Grinding: Influence of CuO Dispersion and Multicycle Operation on DeSO_x Performances. *Appl. Catal. B Environ.* **2016**, *181*, 379–388. [[CrossRef](#)]
49. Gaudin, P.; Dorge, S.; Nouali, H.; Kehrl, D.; Michelin, L.; Josien, L.; Fioux, P.; Vidal, L.; Soulard, M.; Vierling, M.; et al. Synthesis of Cu-Ce/KIT-6 Materials for SO_x Removal. *Appl. Catal. A Gen.* **2015**, *504*, 110–118. [[CrossRef](#)]
50. Xue, M.; Chitrakar, R.; Sakane, K.; Ooi, K. Screening of Adsorbents for Removal of H₂S at Room Temperature. *Green Chem.* **2003**, *5*, 529–534. [[CrossRef](#)]
51. Davenport, W.G.; King, M.J.; Rogers, B.; Weissenberger, A. *Sulphuric Acid Manufacture*; R.T. Jones: Johannesburg, South Africa, 2006; Volume 16.
52. Nelson, S.G. Elemental Sulfur Production from SO₂-Rich Gases. *Coal Sci. Technol.* **1993**, *21*, 543–554.
53. Liu, G.; Gao, P.X. A Review of NO_x Storage/Reduction Catalysts: Mechanism, Materials and Degradation Studies. *Catal. Sci. Technol.* **2011**, *1*, 552–568. [[CrossRef](#)]
54. Poulston, S.; Rajaram, R.R. Regeneration of NO_x Trap Catalysts. *Catal. Today* **2003**, *81*, 603–610. [[CrossRef](#)]
55. Engström, P.; Amberntsson, A.; Skoglundh, M.; Fridell, E.; Smedler, G. Sulphur Dioxide Interaction with NO_x Storage Catalysts. *Appl. Catal. B Environ.* **1999**, *22*, L241–L248. [[CrossRef](#)]
56. Sentürk, G.S.; Vovk, E.I.; Zaikovskii, V.I.; Say, Z.; Soylu, A.M.; Bukhtiyarov, V.I.; Ozensoy, E. SO_x Uptake and Release Properties of TiO₂/Al₂O₃ and BaO/TiO₂/Al₂O₃ Mixed Oxide Systems as NO_x Storage Materials. *Catal. Today* **2012**, *184*, 54–71. [[CrossRef](#)]
57. Nematbakhsh, G.A. Développement de NO_x and NH₃ Potentiometric Sensors for Harsh Environment. Ph.D. Thesis, Mines Saint-Etienne, Saint-Etienne, France, 2020.
58. Zhao, D.; Feng, J.; Huo, Q.; Melosh, N.; Fredrickson, G.H.; Chmelka, B.F.; Stucky, G.D. Triblock Copolymer Syntheses of Mesoporous Silica with Periodic 50 to 300 Angstrom Pores. *Science* **1998**, *279*, 548–552. [[CrossRef](#)] [[PubMed](#)]
59. Mathieu, Y.; Soulard, M.; Patarin, J.; Molière, M. Mesoporous Materials for the Removal of SO₂ from Gas Streams. *Fuel Process. Technol.* **2012**, *99*, 35–42. [[CrossRef](#)]
60. Thommes, M.; Kaneko, K.; Neimark, A.V.; Olivier, J.P.; Rodriguez-Reinoso, F.; Rouquerol, J.; Sing, K.S.W. Physisorption of Gases, with Special Reference to the Evaluation of Surface Area and Pore Size Distribution (IUPAC Technical Report). *Pure Appl. Chem.* **2015**, *87*, 1051–1069. [[CrossRef](#)]
61. Berger, M.; Dorge, S.; Nouali, H.; Habermacher, D.; Fiani, E.; Vierling, M.; Molière, M.; Brilhac, J.F.; Patarin, J. Desulfurization Process: Understanding of the Behaviour of the CuO/SBA-15 Type SO_x Adsorbent in the Presence of NO/NO₂ and CO/CO₂ Flue Gas Environmental Pollutants. *Chem. Eng. J.* **2020**, *384*, 123318. [[CrossRef](#)]
62. Berger, M.; Nouali, H.; Dorge, S.; Habermacher, D.; Fiani, E.; Vierling, M.; Molière, M.; Schönnenbeck, C.; Brilhac, J.F.; Patarin, J. Long-Term Activity of a CuO/SBA-15 Type SO_x Adsorbent: Impact of the Regeneration Step. *Chem. Eng. J.* **2018**, *347*, 202–213. [[CrossRef](#)]
63. Schmitz, P.J.; Baird, R.J. NO and NO₂ Adsorption on Barium Oxide: Model Study of the Trapping Stage of NO_x Conversion via Lean NO_x Traps. *J. Phys. Chem. B* **2002**, *106*, 4172–4180. [[CrossRef](#)]
64. Hess, C.; Lunsford, J.H. NO₂ Storage and Reduction in Barium Oxide Supported on Magnesium Oxide Studied by in Situ Raman Spectroscopy. *J. Phys. Chem. B* **2003**, *107*, 1982–1987. [[CrossRef](#)]
65. Ding, Y.; Wang, S.; Zhang, L.; Lv, L.; Xu, D.; Liu, W.; Wang, S. Investigation of Supported Palladium Catalysts for Combustion of Methane: The Activation Effect Caused by SO₂. *Chem. Eng. J.* **2020**, *382*, 122969. [[CrossRef](#)]
66. Liu, C.; Ma, Q.; Liu, Y.; Ma, J.; He, H. Synergistic Reaction between SO₂ and NO₂ on Mineral Oxides: A Potential Formation Pathway of Sulfate Aerosol. *Phys. Chem. Chem. Phys.* **2012**, *14*, 1668–1676. [[CrossRef](#)] [[PubMed](#)]
67. Lv, L.; Wang, X.; Shen, M.; Zhang, Q.; Wang, J. The Lean NO_x Traps Behavior of (1–5%) BaO/CeO₂ Mixed with Pt/Al₂O₃ at Low Temperature (100–300 °C): The Effect of Barium Dispersion. *Chem. Eng. J.* **2013**, *222*, 401–410. [[CrossRef](#)]
68. Ji, Y.; Toops, T.J.; Graham, U.M.; Jacobs, G.; Crocker, M. A Kinetic and DRIFTS Study of Supported Pt Catalysts for NO Oxidation. *Catal. Lett.* **2006**, *110*, 29–37. [[CrossRef](#)]
69. Liu, Y.; Meng, M.; Zou, Z.-q.; Li, X.-g.; Zha, Y.-q. In Situ DRIFTS Investigation on the NO_x Storage Mechanisms over Pt/K/TiO₂-ZrO₂ Catalyst. *Catal. Commun.* **2008**, *10*, 173–177. [[CrossRef](#)]
70. Anguita, P. Impact Des Biocarburants Sur Le Système d'oxydation Catalytique Des Véhicules Diesel. Ph.D. Thesis, Université Claude Bernard Lyon 1, Villeurbanne, France, 2018.
71. Azambre, B.; Zenboury, L.; Koch, A.; Weber, J.V. Adsorption and Desorption of NO_x on Commercial Ceria-Zirconia (Ce_xZr_{1-x}O₂) Mixed Oxides: A Combined TGA, TPD-MS, and DRIFTS Study. *J. Phys. Chem. C* **2009**, *113*, 13287–13299. [[CrossRef](#)]
72. Adamowska, M.; Krztoń, A.; Najbar, M.; Da Costa, P.; Djéga-Mariadassou, G. DRIFT Study of the Interaction of NO and O₂ with the Surface of Ce_{0.62}Zr_{0.38}O₂ as DeNO_x Catalyst. *Catal. Today* **2008**, *137*, 288–291. [[CrossRef](#)]

73. Shaheen, W.M.; Maksod, I.H.A. El Thermal Characterization of Individual and Mixed Basic Copper Carbonate and Ammonium Metavanadate Systems. *J. Alloys Compd.* **2009**, *476*, 366–372. [[CrossRef](#)]
74. Yamazaki, K.; Suzuki, T.; Naoki, T.; Kouji, Y.; Sugiura, M. Effect of the Addition of Transition Metals to Pt/Ba/Al₂O₃ Catalyst on the NO_x Storage-Reduction Catalysis under Oxidizing Conditions in the Presence Of SO₂. *Appl. Catal. B Environ.* **2001**, *30*, 459–468. [[CrossRef](#)]

Disclaimer/Publisher’s Note: The statements, opinions and data contained in all publications are solely those of the individual author(s) and contributor(s) and not of MDPI and/or the editor(s). MDPI and/or the editor(s) disclaim responsibility for any injury to people or property resulting from any ideas, methods, instructions or products referred to in the content.